DRYING DYNAMICS OF SESSILE DROPLETS ON SUBSTRATES OF DIFFERENT WETTABILITIES

Lanhe Zhang

A thesis presented to the faculty of Mount Holyoke College in partial fulfillment of the requirements for the degree of Bachelor of Arts with Honors

Department of Chemistry

South Hadley, Massachusetts

May, 2012

This thesis was prepared under the direction of Dr. Wei Chen
for 12 credits of independent study

ACKNOWLEDGEMENTS

To my research advisor, Prof. Wei Chen, for being such an incredible teacher, mentor, and friend throughout my years at Mount Holyoke College. Because you always had faith in me, I had the driving force to be persistent in front of obstacles. If I have made any accomplishment, I attribute it largely to you.

To my other thesis committee members, Prof. Maria A. Gomez for seeing my potential and being encouraging very early on since my first year, and Prof. Matthew Noonan, for the genuine support and great insights. It is my great fortune to get to know you and be one of your students.

To my mother, for your unconditional love and belief in my ability to succeed, and for respecting my choice and being proud of me all the time. You are the strongest woman I have ever known; all that I am, or hope to be, I owe it to you.

To Prof. Jayathilake and Dr. Zuniga, for all the suggestions you have made on my research projects; to Shelly Hsiao, for being my peer mentor and passing the project to me; to Marian Rice, for instructing me to operate TEM all on my own; to Dana, Alison, Mojun, Jiaxi, Mimi, My-Lihn, Yen, Wanxin, and Ye. Thank you for all the laughter and food during group meetings and trips.

To Uncle Tong and the Morales, for making me part of your families.

TABLE OF CONTENTS

Page Number

LIST OF FIGURES, TABLES AND SCHEMES

Page Number

ABSTRACT

The interaction between a liquid and a solid substrate, as encountered in any wetting phenomenon, is relevant to a wide range of industrial and biological applications. The drying mechanism was first explored by Deegan and his co-workers through the "coffee-ring" effect.[1,5,6] In the current study, the objectives are to understand the detailed evaporation mechanisms on surfaces of various hydrophobicities and how surface chemical heterogeneity, together with surface physical roughness can dictate the overall deposit patterns of sessile droplets.

The dynamics of the three-phase contact line of sessile droplets containing poly(vinyl alcohol) adsorbed gold nanoparticles is experimentally investigated on three silica substrates – silicon wafer, quartz, and glass – with different surface roughness and chemistry. Substrate and particle surface chemistry modulate surface-particle and particle-particle interactions and affect how particles pack relative to their nearest neighbors. In addition, it was found that substrate surface chemistry and roughness play significant roles in controlling the extent of contact line pinning and affecting particle distribution in a deposit. Our hypothesis that the total intrinsic energy barrier for contact line pinning consisting of three components, U_{pr}, U_{ch} and $U_{\mathrm{p-s}}$, created by substrate physical roughness, chemical heterogeneity and particle-substrate interactions, respectively, has been tested successfully based on experimental observations. This extension of preexisting theory can be used as a guide to analyze more complicated systems and predict the behavior of an evaporating droplet on a solid substrate.

1. INTRODUCTION

1.1 From the "Coffee Ring"

A ring-like stain is commonly observed as a spilled coffee drop dries on a solid surface. Such dark rings form whenever droplets containing suspended particulate matter evaporate on a substrate. This phenomenon, known as the coffee ring effect,[1] is familiar to people as a common drying process but its great implications are realized only a decade ago. The challenge comes from the fact that the accumulation of materials at the contact line results in an uneven distribution of solute particles - the ring (see Figure 1). In applications such as coating, painting and printing, it is required to produce a uniform deposition of material by evaporation.[2,3] Meanwhile, the microscopic organization of individual particles into ordered patterns is also important.[4] The process of evaporation of a sessile droplet governs the final deposit pattern. In addition to a sufficient understanding and an accurate description of the underlying phenomena, the ability to engineer the supporting material to control the deposit pattern is highly desirable.

Figure 1. A drop of coffee forms a perimeter ring upon drying.[1]

Upon drying, rather than forming a uniform spot, a ring of solute deposits on the periphery of the droplet. Deegan and his co-workers first showed that the rate of evaporation of a sessile droplet is not uniform across the droplet surface and is maximized at the edge of the drop.[1, 3, 4] The contact line is pinned during the drying process so that liquid evaporating from the edge must be replenished by liquid from the interior (called the convective flow), leading to the migration of solutes to the contact line and finally ring formation.[1-6] The drying process is illustrated in the left image of Figure 2.

Notice there is a concurrent Marangoni flow generated by a concentration or a surface tension gradient (see the right image of Figure 2).[7,8] This effect is usually observed in a solution containing two kinds of solvents with different surface tensions and boiling points. The magnitude of the Marangoni flow is determined by the Marangoni number:

$$M = \frac{\Delta\gamma L}{\mu D_{AB}}$$

where $\Delta\gamma$ denotes the surface tension difference between the center and edge of the droplet, μ is the viscosity of the mixed solvent, L is the length scale involved (i.e., the radius of the microdroplet placed on the substrate), and D_{AB} is the diffusion coefficient in the binary solution.[9] Therefore, by introducing a proper second solvent into the solution, a Marangoni flow in the opposite direction of the convective flow can be achieved; particles near the periphery can be brought back and redistributed in the central area. Ever since Deegan's work on evaporating

sessile droplets, a lot of efforts have been devoted to understanding more precisely the shape of the deposit, the pinning/depinning processes, the effect of particle concentration and the dynamics of the dispersed solute particles.[10-16] Until very recently, it is also found that adding elliptical particles into the colloidal system can produce uniform deposition due to their anisotropic shape.[17]

Figure 2. Cross-sectional view of the droplet profiles. Left: the nonuniform distribution of evaporation flux along the surface is represented by the length of the arrows above the droplets. Right: hydrodynamic flows generated by inward Marangoni effect (indicated by the orange lines).[8]

1.2 Wetting Phenomena

The current study focuses on the investigation of both the macroscopic deposit pattern and the microscopic distribution of individual particles across the deposit region. To promote an overall even distribution of particles macroscopically, several factors including convective and Marangoni flows discussed above must be taken into consideration. For a simple aqueous system, the convective flow is commonly experienced but the Marangoni flow is mostly suppressed. Moreover, it is important to emphasize the important role played by substrate surface chemistry that can control solute-substrate interactions and modify the extent of contact line pinning. In short, the goal is to understand how substrate surface chemistry can impact the final deposition of an evaporating droplet.

One of the characterizing properties of a solid substrate is its wettability, which can be quantified by contact angle measurement. In literature, two distinctive drying mechanisms are established based on substrate wettability: a droplet dries with a constant contact area and decreasing contact angle (see left image of Figure 3) or with a constant contact angle and decreasing contact area (see right image of Figure 3).[19] In the initial stage of drying, contact angle of the droplet decreases while maintaining contact area as water evaporates until the receding contact angle (θ_R) is reached. On hydrophilic surfaces where θ_R is low, the contact line is pinned soon after deposition due to the strong attractions between the substrate and the solvent, while contact angle keeps decreasing. On the other hand, on hydrophobic surfaces where θ_R is high, the contact line keeps receding during most of the drying process; the resulting micropatch could concentrate particles to the middle of the drop. Depending on the hydrophilicity/hydrophobicity of the substrate, the droplet can exhibit either complete or partial wetting. Figure 3 illustrates these two extreme modes of evaporation. In between these two extremes, "stick-slip" motion is also commonly observed.[20, 23-25] As evaporation continues, the capillary force pulls the liquid inward and the contact line becomes depinned, maintaining its receding contact angle at the meantime. The contact line slips and reaches another equilibrium position where it is pinned again. This "stick-slip" motion can be repeated, leaving concentric rings on the substrate.
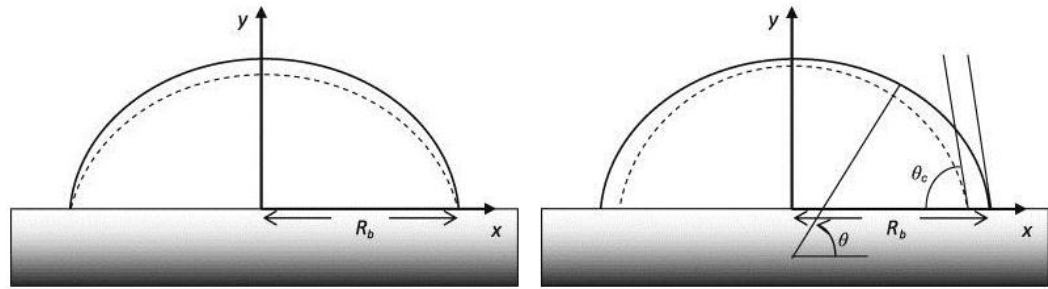
Figure 3. Cross-sectional view of (a) constant contact area mode and (b) constant contact angle mode. Solid lines indicate droplet profiles after initial deposition. Dashed lines show the profile progression at a later time.[18]

1.3 Contact Angle and Young's Equation

A significant portion of this work focusing on surface chemistry is devoted to the study of substrate wettability. Wetting is the ability of a liquid to maintain contact with a solid surface, the degree of which can be determined quantitatively by contact angle measurement. The contact angle (θ_0), as seen in Figure 4, is the angle at which the liquid-vapor interface meets the solid-liquid and solid-vapor interfaces and is a result of force balance between adhesive and cohesive forces. For an ideal solid substrate that is flat, rigid, chemically homogeneous and perfectly smooth, the contact angle for a sessile drop at equilibrium is given by the Young's equation:

$$\gamma cos\theta_0 = \gamma_{SG} - \gamma_{SL}$$

where θ_0 is the equilibrium/static contact angle, γ is the liquid surface energy, and γ_{SG} and γ_{SL} are the solid-vapor and solid-liquid surface energies, respectively (See Figure 4).[22] In practice, chemical inhomogeneity of the solid substrate and

the existence of surface defects can lead to significant deviation of the equilibrium contact angle from the ideal one. This necessitates the use of dynamic contact angles, both advancing and receding contact angles. They are respectively measured when liquid is added to and withdrawn from the droplet. The difference between the advancing (θ_A) and receding (θ_R) contact angles is termed hysteresis (H), which provides an indication of the deviation from the ideal surface:

$$H = \theta_A - \theta_R$$

In the work presented here, both dynamic contact angles and static contact angles were measured on various substrates to examine their impact on the drying behavior of sessile droplets. Moreover, dynamic contact angle measurements and surface hysteresis calculations serve as a ruler to quantify the net effect of surface physical roughness and chemical heterogeneity.
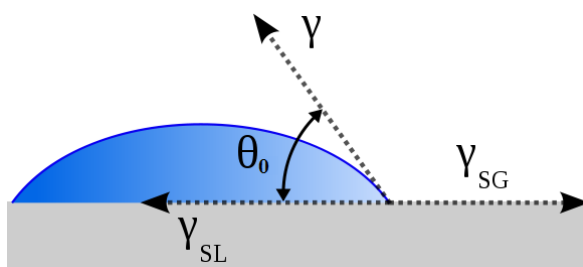
Figure 4. A sessile droplet sits on a solid substrate. θ_0 represents the equilibrium contact angle formed at the solid/liquid/gas interface.[22]

1.4 Nanoparticle Self-assemblies at Interfaces

The drying of drops of colloidal suspension is a crucial step in many applications and the drying behavior of different colloids has been studied, such as mixed oxide colloids and micro-scale polymer beads.[15,26] The study of drying patterns of sessile droplets containing nanoscale gold particles was chosen because fabrication of nanocomposites containing metallic nanoparticles with well-defined dimensions and structures is the most important step toward utilization of their unique properties in sensing, catalysis and magnetic storage. Therefore, creating periodic assembled nanostructures has attracted significant attention in the scientific community.[27-29]

Gold nanoparticles are of special interest for several reasons. First, they possess distinct optical properties. These finely-divided colloids were discovered as far back as the 5th century and have been applied to surfaces of fabrics, chinaware and enamels to generate a glittering effect.[30] Bulk gold presents a familiar yellow color whereas gold nanoparticles have various colors depending on the size of individual particles. The size-dependent optical properties of gold nanoparticles stem mainly from their high surface-to-volume ratio and quantum size effect.[31, 32] Characteristically, gold nanoparticles in the 5-20 nm diameter range exhibit a strong absorption band in the visible region near 520 nm. This strong absorption of green light gives gold nanoparticles their intense ruby-red color. Secondly, gold is one of the very few metals noble enough to survive as a

nanoparticle under atmospheric conditions.[33] Experimentally, gold nanoparticles of 15 nm in diameter are easily synthesized through citrate reduction. This method produces monodisperse colloidal particles whose size depends on the ratio of initial concentrations of citrate to gold precursor.[34,35] The system can remain stable over a long period of time because of the electrostatic repulsion produced by negatively charged citrate ions on the surfaces of gold nanoparticles. Thirdly, closely packed gold nanoparticles cause the absorption spectra to red shift, the extent of which depends on the interparticle distance and aggregation state. As a result, the deposit patterns of gold nanoparticles show distinct colors under optical microscopy. Therefore, information about macroscopic particle distribution can be extracted simply from color changes. Finally, gold nanoparticles have many important applications such as cellular imaging and catalysis.[36] Until very recently, unexpected magnetism in gold nanostructures is also discovered.[37]

In general, nano-organization can be achieved using "top-down" or "bottom-up" approaches.[38] Top-down approaches seek to create nanoscale devices by using larger, externally-controlled tools to shape materials into the desired shape and order. Micropatterning techniques, such as lithography and inkjet printing, belong to this category.[39,40] Bottom-up approaches, in contrast, use physical and chemical properties of certain molecules or molecular complexes to self-organize or self-assemble into macrostructures. As a result, specific non-covalent interactions are instrumental in leading to spontaneously formed architectures.[41, 42] The organization of these molecular building blocks is driven

by a combination of thermodynamic and kinetic factors. Nonlithographic approaches based on thermodynamically driven self-assembly processes are easy, fast and economical in constructing large-scale nanoparticle organizations. The fabrication of functional, aggregation-free, two-dimensional nanoparticle arrays with tunable size and inter-particle spacing typically utilizes a variety of techniques described below.

Evaporation-induced assembly of nanoparticles suspended in liquid is the simplest method to order particles on surfaces.[43] Subjected to slow and irreversible evaporation of solvent molecules, solute nanoparticles can potentially form well-ordered patterns on substrates. In general, nanoparticles are considered as uniformly dispersed in the liquid upon deposition. The general drying mechanism discussed at the beginning applies to particles on a nanoscale: as the drying front moves on a surface, nanoparticles dispersed in the solution are pulled towards the drying front by convective flow and then deposited there as the drying front retracts. Ideally, particles would deposit and self-assemble as a two-dimensional monolayer at the interface, as shown in Figure 5.
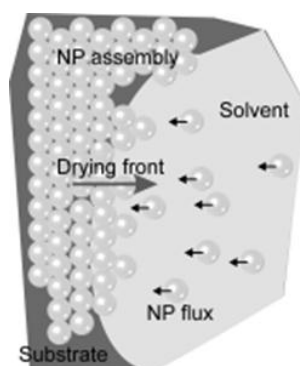

Figure 5. Drying-mediated assembly of nanoparticles on surfaces.[38]

In the work presented here, the convenient setting of solvent-evaporation-induced self-assembly was taken advantage of. Droplets were cast on planar surfaces with various wettabilities. Strong van der Waals attractions between the metallic nanoparticles and the substrate are known to play a key role in the self-organization behavior; as discussed previously, these forces can be adjusted through modifications of the supporting material. In addition, a capillary force is applied by the surface tension of the evaporating solvent.[44] This force is attractive between similar particles, bringing particles closer and producing two-dimensional structures. When a colloidal particle sits at a liquid/air interface, the latter is usually deformed in the vicinity of the particle. The menisci thus engendered by two particles give rise to this lateral capillary force. Depending on the physical origin of the interfacial deformation, several kinds of lateral capillary forces are generated, two of which are illustrated in Figure 6. In Figure 6 (a), the deformation around two floating particles is due to gravitational effects and thus induces a lateral capillary force. To produce a significant interfacial deformation, the particles normally have diameters greater than 5-10 μm. For smaller particles on the nano-scale, the effect of the gravitational field becomes negligible. As in Figure 6 (b), capillary interaction appears also when the particles are immersed in a liquid film. In this case, the interfacial deformation is related to the wetting properties of the particle surface rather than to gravity. This immersion capillary force is mainly responsible for clusters and long-range ordered two-dimensional domains.

Due to their large surface-to-volume ratio and high surface energy, nanoparticles dispersed in a liquid tend to aggregate over time, especially in the case of highly concentrated colloids. Upon deposition, nanoparticles subjected to the strong immersion capillary force are brought closer to each other, becoming even more susceptible to aggregation. This force is mainly responsible for the formation of nanoparticle clusters, and thus destroys ordered nanoparticle arrays.[44]
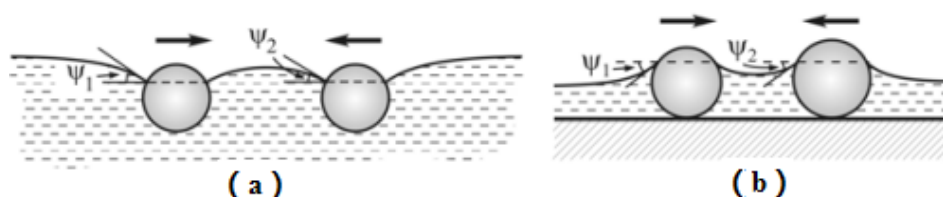
Figure 6. Lateral capillary forces between particles attached to liquid interfaces. (a) Force between two floating particles. (b) Force between particles captive in a liquid film.[44]

1.5 Polymer-Nanoparticle Composites

Adding nanoparticulates to a polymer matrix can potentially solve this problem and enhance their performance at the same time.[45,46] On one hand, nanoparticles need to be protected against coagulation in order to maintain many of their unique properties. On the other hand, the polymer nanocomposite requires uniform dispersion of nanoparticles in the polymer matrix for structural applications. The macromolecules adsorbed onto the surfaces of nanoparticles provide steric repulsion to neighboring particles and effectively prevents particle

aggregation. In addition, free polymer molecules in solution also prevent neighboring particles from coagulation. Gold nanoparticles are known to have strong affinities for thiol and amine functional groups.[47,48] Poly(amido amine) (PAMAM) dendrimers functionalized with thiol termini were reported to stabilize 2 nm gold nanoparticles dispersed in organic solvents. Due to the sensitivity of surface plasmon to boundary changes, these molecular ligands were detected based on the change in the absorption spectra.[49] Together with providing stabilization to the colloidal system, polymers are employed as ligands to control nanoparticle spatial distribution. The distance between nanoparticles is normally manipulated by adjusting polymer molecular weight. For example, carboxyl-functionalized poly(dimethylsiloxane) (PDMS) ligands were attached to nanoparticle surfaces; thiol end-functionalized polystyrene chains were introduced onto the surface of gold nanoparticles, which self-organized into hexagonally ordered monolayers when cast onto solid substrates.[50,51]

In this study, poly(vinyl alcohol) (PVOH), $(-CH_2-CH(OH)-)_n$, was chosen as the surface adsorbing molecules on gold nanoparticles for its excellent film forming properties and nontoxicity. The former stems from a combined action of the polymer's crystalline and amorphous domains.[52] Its biocompatibility makes it safe for biomedical applications.

PVOH is among the macromolecules that can adsorb onto gold nanoparticles and provide steric stabilization to prevent particle aggregation. This

polyhydroxy polymer is a synthetic polymer. PVOH cannot be prepared by polymerization of the corresponding monomer because vinyl alcohol almost exclusively exists in its tautomeric form, acetaldehyde. Therefore, it is commercially manufactured by the polymerization of vinyl acetate, followed by hydrolysis of poly(vinyl acetate) to partially or completely convert acetate to alcohol groups.[53] As a result, the molecular weight and the degree of hydrolysis of this polymer can vary over a wide range, which in turn affects its physical properties. PVOH has a melting point of 230 °C and 180-190 °C for the fully hydrolyzed and partially hydrolyzed grades, respectively. The glass transition temperature of fully hydrolyzed PVOH has been determined to be 85 °C. In general, PVOH has good water solubility and biocompatibility, as well as the ability to crystallize and hydrogen bond. Typically, PVOH is only soluble in highly polar solvents, such as water and dimethylsulfoxide. Its solubility in water is a function of the degrees of polymerization (DP) and hydrolysis (Figure 7).[54]
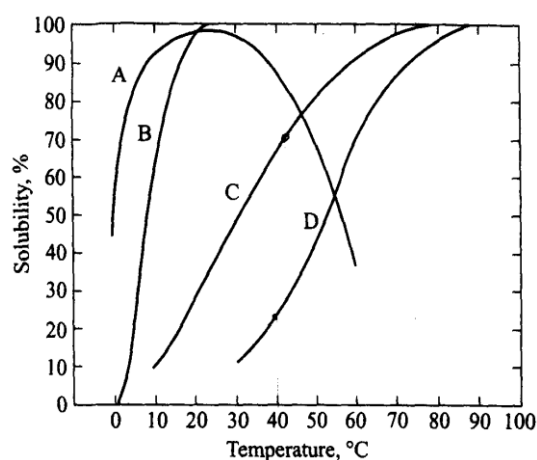

Figure 7. Water solubility of PVOH grades: A, 78-81% hydrolyzed, DP=2000-2100; B, 87-89% hydrolyzed, DP=500-600; C, 98-99% hydrolyzed, DP=500-600; D, 98-99% hydrolyzed, DP=1700-1800.[54]

Adsorption is energetically favorable as the process lowers the high surface energy of gold nanoparticles, decreasing the enthalpy of the system. Adsorption also causes a loss in the conformational entropy of the polymer, being energetically unfavorable on the other hand. Accordingly, the final conformation of the adsorbed PVOH is governed by the law of thermodynamics for spontaneous reactions, $\Delta G = \Delta H - T\Delta S$.[55,56] Previous work has shown that initial adsorption takes less than 10 min. The resulting configuration rearranges in the next couple of hours and then remains stable over a long period of time. For all the polymer samples examined (molecular weights ranging from 13 k to 186 k and degrees of hydrolysis ranging from 80% to 99%), adsorption kinetics is not influenced by either molecular weight or degree of hydrolysis. Generally speaking, three steps are involved in the formation of an adsorption layer: (1) diffusion of the adsorbate toward the surface, (2) attachment of the adsorbate onto the surface, and (3) rearrangement of the adsorbate on the surface.[57] However, the binding mechanism and ultimate configuration of the gold nanoparticle-PVOH complex depend on the polymer composition and the relative sizes of the adsorbate and adsorbent. While details of adsorption are still under active investigation in the group, it has been found that, for PVOH samples with a chain size smaller than the diameter of the nanoparticles, the adsorption thickness is rather comparable to the free polymer size. In this case, it is very likely that the nanoparticle surface is saturated with polymer chains, of which the conformation is almost identical to that of the free chains with little loss of conformational entropy. When the

polymer diameter is much larger than that of the nanoparticles, each polymer

chain can wrap itself around a single nanoparticle, and thus the dimension of the

entire conjugate resembles that of the free polymer (See Figure 8).
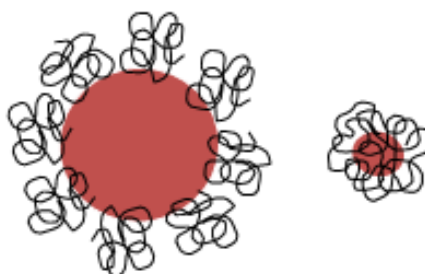
Figure 8. Schematic models of stable adsorption configurations. Left, the dimension of adsorbed polymer is smaller than that of the particle; right, the dimension of adsorbed polymer is larger than that of the particle.

More interestingly, adsorption of PVOH from aqueous solution onto

hydrophobic surfaces is a general phenomenon that can be used for surface

modification. It is reported that PVOH irreversibly adsorbs onto almost any

hydrophobic surface, producing robust hydrophilic coatings.[58,59] It has been

shown that the initial steps of adsorption/crystallization at hydrophobic

surface/water interfaces are driven by hydrophobic interactions or displacement of

water molecules from the interface, lowering interfacial free energy. However,

previous studies indicate that PVOH molecules might exist in different

configurations, depending on the humidity of the surrounding environment. At

high humidity, more water is retained in the adsorbed PVOH layer and the

hydroxyl groups in PVOH are likely to be exposed to the polymer/air interface.

Therefore, under a humid environment, the PVOH surface appears slightly more hydrophilic.

1.6 Solvent Selection

Most studies focus either on metal nanoparticles dispersed in non-polar organic solvents (typically hexane or toluene) or on self-assembled nanostructures synthesized through complex phase transfer processes.[60,61] Upon evaporation, ordered monolayer assemblies of surface-modified nanoparticles are easily made, taking advantage of the lateral capillary force discussed above. Notice that the solvents applied all have low surface tension. For instance, at 20 °C, toluene has a surface tension of 28.5 dyn/cm and it is 18.4 dyn/cm for *n*-hexane. The low surface tension exerts a capillary force to be counter-balanced by the short-range repulsions due to the adsorbed ligand molecules. However, organic solvents are toxic in general and are thus not favorable for biological applications.

In our study, water is chosen as the solvent for its ubiquity and environmental benignity. Water, on the other hand, has a relatively high surface tension of 72.8 dyn/cm at 20 °C. Consequently, instead of forming well-ordered hexagonal patterns, a larger lateral capillary force, caused by the solvent's higher surface tension, tends to result in particle aggregations. In this study, PVOH samples exhibiting a relatively narrow molecular weight distribution of 13~23k serve as the "soft" coating material to stabilize gold colloids and to provide desired interparticle spacing for self-assembly. Under similar drying conditions, a

perfectly ordered pattern should be a joint effect of several factors including particle-particle, particle-solvent and particle-substrate interactions. Substrate surface chemistry comes into play as it can potentially modulate all kinds of interactions at the interface and direct particle packing relative to their nearest neighbors.

1.7 Project Objectives

The goals of the project are to understand the detailed evaporation mechanisms on surfaces of various hydrophobicities and how surface wettability dictates the overall deposit patterns of sessile droplets. The dynamics of the three-phase contact line was experimentally investigated on these surfaces. By adjusting surface chemical compositions and topography, a wide range of surface wettabilities were achieved, including complete wetting, partial wetting and non-wetting. Upon drying, both water and aqueous droplets containing concentrated gold nanoparticle-PVOH conjugates served as sessile droplets. Using pure water droplet as a control, the effect of the addition of solid nanocomposites in the drying process was elucidated. By constructing droplet profiles which show the evolutions of both contact radius and contact angle with time, a comprehensive picture for an evaporating droplet observed visually under an optical microscope was presented.

It is also realized that substrate physical roughness as well as chemical heterogeneity cause contact angle hysteresis and thus complicate the

understanding of the wetting behavior of liquids on solids. To address these issues, three kinds of supporting materials (silicon wafers, quartz slides and glass slides) were chosen. These substrates were used because of their similar surface chemistry and complementary physical characteristics, as summarized in Table 1. Dynamic contact angle measurements were carried out using water as well as concentrated colloidal solutions as probe liquids. It is clear that the dynamics of the contact line of wetting systems accompanied by evaporation is a complex problem. Moreover, in the presence of solid nanoparticles, the situation is even more complex. On non-ideal surfaces, the pinning and depinning forces should result from a combined effect of surface hydrophilicity, surface chemical and physical heterogeneities, and addition of nanoparticles. The dominating factor among these surface properties was identified and rationalized.

Table 1. A comparison of different substrate materials used for droplet.

	Chem. Comp.[*]	State of Existence	Physical Homogeneity	Chemical Homogeneity	Characterization Instrument
Silicon Wafer	Si/SiO$_2$	Amorphous	Smooth	High -OH Density	-AFM -Ellipsometry -Contact Angle Goniometer
Fused Quartz Slides	SiO$_2$	Amorphous	Relatively Smooth	Low -OH Density	-AFM -Optical Microscope -Contact Angle Goniometer
Glass Slides	SiO$_2$	Amorphous	Very rough	Medium -OH Density	-Optical Microscope -Contact Angle Goniometer

Chem Comp.[*]: Chemical Composition

2. EXPERIMENTAL

2.1 Materials and Apparati

*General. P*oly(vinyl alcohol) (PVOH) (MW = 13-23 kDa and 98% hydrolyzed; MW = 89-98 kDa and 99+% hydrolyzed) powder, hydrogen tetrachloroaurate (HAuCl$_4$) (FW = 393.83 kDa, 99+% pure) and acetyl chloride (FW = 78.50 Da, b.p. 50-52°C, 99+% pure) were purchased from Sigma-Aldrich, Inc. Tridecafluoro-1,1,2,2-tetrahydrooctyl-dimethylchlorosilane (FW = 440.70 Da, b.p. 189-91°C, 99+% pure) and heptafluorobutyryl chloride (HFBC, FW = 232.49 Da, b.p. 39°C) were obtained from Gelest and Sigma-Aldrich, Inc., respectively, and were packaged under nitrogen prior to usage. Sodium citrate (FW = 294.10 Da) and organic solvents including toluene, acetone, and ethanol were attained from Fisher Scientific, Inc. All reagents were used as received without further purification. Water was purified using Millipore Milli-Q Biocel System (Millipore Corp., resistivity ≥ 18.2 MΩ/cm). Substrate materials such as silicon wafers (100 mm in diameter, P/B doped, resistivity 1-10 Ω-cm, thickness 475-575 μm) were purchased from International Wafer Service, Inc. Microscope cover glass slides (18 mm in diameter) were obtained from Fisher Scientific, Inc. Ground and polished quartz plates (1.56 mm in thickness) were purchased from Chemglass. All glassware was cleaned in a base bath containing potassium hydroxide and isopropyl alcohol, rinsed with deionized water and dried/stored in an oven at 110 °C.

Instrumentations. Dynamic Light Scattering measures Brownian motion and relates it to the hydrodynamic size of the particles, typically in the sub-micron region. The size distribution analyses of lab synthesized gold nanoparticles, PVOH chains and their conjugates were performed using a Malvern Zetasizer Nano-S instrument, equipped with a 4 mW He-Ne laser ($\lambda = 632.8$ nm). Refractive indices of PVOH (n = 1.520) and water (n = 1.330) at 25°C were assigned to calculate particle dimensions. In addition, viscosity of water at 25°C, $\eta = 0.8872$ cP, was assigned as the solution viscosity. To obtain concentrated colloidal solutions, centrifugation of colloid-polymer suspensions was performed using an AccuSpin Micro 17R Microcentrifuge (24-Place Rotor, Fisher Scientific, Inc.).

Clean surfaces at an atomic level are particularly important when surface bonding or coating is required. Oxygen plasma was applied on silicon wafer, glass and quartz substrates to achieve ultra-clean surfaces. Surface cleaning for all supporting substrates was performed using Plasma Cleaner PDC-001 (Harrick Scientific Corp.). To obtain thickness information on silicon wafers, a LSE Stokes Ellipsometer (Gaertner Scientific Corp.), equipped with a 1 mW He-Ne laser ($\lambda = 632.8$ nm) was utilized. The angle of incidence from the normal to the plane is 70°. Thickness measurements were based on the following parameters: air, $n_0 = 1$; silicon oxide with surface modified layers, $n_1 = 1.457$; silicon substrate, $n_s = 3.882$. Measurement error is within 1 Å as specified by the manufacturer unless specified otherwise. The thickness of silicon wafer substrate was measured before and after

each step of surface modification. Hence, the difference between the two
measurements provides the thickness of each newly built surface layer. The
reported thickness was an average of four measurements made on different areas
of each sample surface.

To better characterize surface features, atomic force microscopy (AFM),
which can image surface topography at nanoscopic resolution, was used. Images
of both silicon wafer and quartz substrates were obtained using a Veeco
Metrology Dimension 3100 AFM (Veeco Instruments, Inc.) under tapping mode
with a Veeco silicon tip (resistivity 1-10 Ω-cm, P doped). AFM images were
analyzed using the Nanoscope software (Veeco Instruments, Inc.). Three-
dimensional topography, two-dimensional height and phase profiles, as well as
root-mean-square roughness of images were determined.

Surface wettability was measured by contact angle goniometry.
Measurements were made using a NRL C.A. 100-00 goniometer (Ramé-Hart
Instrument Co.) with a Gilmont syringe (Gilmont Instrument Co.) and a 24-gauge
flat-tipped needle. Dynamic contact angles were measured on all substrates after
each step of surface modification. The probe fluids used were Milli-Q water and
concentrated (x10) colloid-polymer solution. Advancing contact angle (θ_A) and
receding contact angle (θ_R) were recorded respectively as the probe fluid was
added to and withdrawn from the drop. On each sample substrate, three spots
were chosen for dynamic contact angle measurement and the average of the

measurements was reported to quantify surface wettability. Within the same batch

of samples, the standard deviation of reported values was less than or equal to 2°

unless specified otherwise.

Droplet profiles were recorded during the process of evaporation under

ambient atmosphere using an Olympus BX51 microscope (Olympus Corp., Japan).

The optical microscope was equipped with an Olympus DP70 (Olympus Corp.,

Japan) digital camera capable of capturing up to 1000 snapshots and compiling

them into a time-lapse video. In addition, the DP70 software package including

DP controller and DP manager was used to analyze images taken for an

evaporating droplet.

2.2 Methods

Preparation of PVOH solutions. 0.1 wt% PVOH solutions were prepared

by dissolving PVOH powder in Milli-Q water. A 150 mL polypropylene plastic

bottle was filled with Milli-Q water and heated in a boiling water bath twice, for

one hour and then for half an hour. The bottle was then thoroughly rinsed with

Milli-Q water prior to the introduction of PVOH powder and Milli-Q water for

PVOH solution preparation. Dissolution was performed by stirring the solution in

a hot water bath maintained at 95 °C for three hours. The resulting solution was

allowed to cool overnight with mild stirring. An extra day or two was needed

(without stirring) for the solution to reach equilibrium and stability. Due to the

aggregation of PVOH chains over time, solutions were utilized within 3 months of preparation.

Gold nanoparticle synthesis. Using the citrate reduction method,[35] 50 mL of 0.25 mM $HAuCl_4$ solution in a 100 mL round bottom flask equipped with a condenser was heated to boil in a water bath. 2 mL of 1 wt% sodium citrate was added quickly to the boiling $HAuCl_4$ solution. Nucleation started immediately as the solution turned from yellow to blue. Heating and stirring the mixture was continued until the final color of the colloidal solution changed from purplish red to deep red. The solution was allowed to cool for 1.5 hours under stirring so that the color of the solution was completely stabilized.

DLS studies. To determine the size distribution of small particles and polymers in solution, ~ 0.8 mL of sample solution was placed in a low-volume disposable polystyrene cuvette (10×4×45 mm) and allowed to equilibrate for 4 min at 25 °C. Fixed position measurement was set at 4.65 mm from the bottom of the cuvette. Measurements of both gold nanoparticles and PVOH chains were made before mixing to make sure there were no aggregates. Occasionally, the size distribution by intensity (αD^6) showed extra peak(s) greater than 100 nm in diameter (D). The monodispersity of the solution was assumed if the same peak(s) were absent in the size distribution plot by volume (αD^3).

Preparation of concentrated solutions containing gold nanoparticle-PVOH conjugates. To prepare nanoparticle-polymer composites, a PVOH

solution (MW = 13-23 kDa and 98% hydrolyzed; 0.1 wt%) was added to a gold

nanoparticles solution in a 4:1 ratio by volume. The mixture was allowed to

equilibrate for 24 hours to permit the adsorption of PVOH chains onto gold

nanoparticle surfaces. 1.5 mL aliquots of gold nanoparticle-PVOH suspension

were centrifuged for 30 min at 13,200 rpm and 20 °C followed by removal of the

supernatant. A dense pellet remained at the bottom of each microtube.

Approximately 1.5 mL of Milli-Q water was added to the tube to redisperse the

conjugate pellet. The suspension was precipitated three more times as described

above in order to remove excess free polymer chains from the aqueous solution.

After the last round of centrifugation and decantation of the supernatant, Milli-Q

water was added to resuspend the pellet to give the desired final concentration. In

the current study, the final pellets were prepared to be 10 times and 150 times

more concentrated than the initial concentration. The concentrated conjugates

were allowed to equilibrate for at least 2 hours. Samples were stored in sealed

microtubes in a dark and cool place to minimize solvent evaporation.

Cleaning of supporting substrates. Silicon wafers and quartz slides were

cut into 1.3×1.5 cm and 1.2×1.3 cm rectangular pieces, respectively. Silicon

wafers and glass cover slides were rinsed with copious amount of house-purified

water, dusted using compressed air and then dried in a clean oven at 110 °C for 30

min. Quartz slides were rinsed with acetone and ethanol prior to Milli-Q water

rinse and oven drying. All samples were placed in a glass petri-dish and

introduced to a radio-frequency (R.F.) plasma chamber. The chamber under

vacuum was flushed with oxygen three times before plasma treatment was performed at a working pressure of ~200 mTorr for 15 min under high power (30 W). By introducing oxygen gas into a vacuum chamber and exposing it to a high R.F. field, ionized oxygen molecules as well as radicals were generated. The excited oxygen species oxidize surface organic molecules by breaking the C-H and C-C bonds to form water vapor and CO_2, which are then evacuated from the chamber via the vacuum pump. Immediately after plasma treatment, the samples were covered and allowed to neutralize in the chamber for 10-15 min in order to minimize electrostatic interactions with contaminants in air. Plasma treatment also maximizes silanol group (Si-OH) density on substrates for further reactions.

Vapor phase silanization. Silanization using tridecafluoro-1, 1, 2, 2-tetrahydrooctyl-dimethylchlorosilane was carried out immediately after plasma treatment. Clean substrates were transferred to a clean glass holder, placed in a custom-designed Schlenk tube. Silanization was performed in the vapor phase at 70 °C in an oil bath for 24 hours using 0.5 mL of the silane reagent. There was no contact between the liquid silane and the substrates. After silanization, the glass holder was transferred to a Schlenk tube filled with toluene. Moving the holder up and down gently to remove the unreacted silane reagent depositing on the surfaces of all substrates. Samples soaked in toluene were then rinsed individually with toluene (2×), acetone (2×), ethanol (2×) and water (2×) (in this order). Water droplets remaining on each substrate was gently blown off with nitrogen gas and

samples were dried in an oven at 110 °C for 10 min. Two samples of each type were used for characterization by ellipsometry, contact angle, and AFM.

PVOH adsorption. Silanized samples were submerged in PVOH solution (MW = 89-98 kDa and 99+% hydrolyzed; 0.1 wt%) at room temperature for 24 hours. Out of concern that some deposition of free polymers might occur when samples were removed through the solution-air interface, the solution was diluted three times with Milli-Q water after adsorption was finished. All samples were then removed, rinsed with copious amounts of deionized water and dried under a stream of nitrogen for at least 30 min and placed in a desiccator overnight. PVOH molecules adsorbed onto the hydrophobic silane layer were allowed to rearrange to achieve the most stable configuration.

Labeling with heptafluorobutyryl chloride (HFBC). After PVOH adsorption, the substrates were reacted with HFBC for 24 hours in the vapor phase at room temperature. Substrates with PVOH layers were transferred to a clean glass holder and placed in a custom-built Schlenk tube fitted with an o-ring and a Teflon stopcock. As a reagent reactive to water, HFBC was transferred to the receiving tube under nitrogen to avoid the introduction of water from the ambient environment. The reaction tube was purged with nitrogen gas for 15 min before 0.5 mL of HFBC was introduced to the tube under nitrogen via cannula transfer, an air-free technique. After 24 hours, samples were rinsed with an excess

amount of deionized water and nitrogen-dried for at least 30 min prior to characterization and further experimentations.

Observation of evaporating sessile droplets and data analysis. Different liquids were used as sessile drops: deionized water and solutions of concentrated (×150) gold nanoparticle-PVOH conjugates. Small droplets of known volumes, ca. 1.5 µL, of the various liquids were gently deposited on supporting materials (silicon wafer, glass slide and quartz slide) with different surface chemical compositions. All observations of the evaporating behavior of a sessile droplet were made in air at ~20-25% humidity and ~22 °C. After being deposited on a substrate, the droplet was left to evaporate until it dries completely. The evolution of the static contact angle, θ, versus time, t, was recorded via the contact angle goniometry every 30 s. Under the optical microscope, droplet profile images were taken every 30 s. For each image, four diameter measurements were made at different locations and averaged by ImageJ; the deviation from the circular contact line can be inferred from the magnitude of the standard deviation of the averaged value. Plots of the evolution of both static contact angle and contact diameter as a function of time were presented to illustrate the complete drying process. To visualize the pinning and depinning process of an evaporating sessile droplet, snapshots of the droplet profile were also recorded every second and compiled into a time-lapse video.

3. RESULTS AND DISCUSSION

3.1 A Revisit to Substrate Selection

Our objective is to study the effects of substrate surface chemistry,

chemical and physical heterogeneities on drying dynamics. We chose three silica

substrates, silicon wafer, quartz and glass. Native substrates of these share similar

surface chemical composition and homogeneity. All three types of substrates have

silanol groups to allow silane attachment and subsequent chemical

transformations. Substrate roughness increases from silicon wafer, quartz, to

glass, allowing the probing of the effect of physical roughness. Assuming a

uniform monolayer formed on all three substrates, the roughness of native silicon

wafer and quartz can be compared through root mean square (RMS) values of the

silanized correspondents. From the RMS values in Appendix 1, it is inferred that

on average, native quartz is physically rougher than silicon wafer by 0.4 nm, due

to manufacturing defects. Glass, on the other hand, is so rough that is beyond the

imaging limit for AFM.

Surface chemistry on silica substrates is relatively straightforward

(Scheme 1) so that substrates with low and high surface energies (or high and low

contact angles) can be prepared. Complementary characterization techniques can

be performed on these substrates due to their differences in optical transparency

as well as physical roughness. Atomically smooth surface and refractive index

difference between the thin oxide layer and the bulk silicon allow reactions on

silicon wafers to be readily monitored using AFM, ellipsometry, and contact

angle goniometry. The polished quartz slides have nanoscopically smooth surfaces that are within the imaging limit for AFM while glass slides are too rough to be imaged. Therefore, smooth silicon wafer and quartz substrates allow AFM to characterize their chemical homogeneity and compare physical roughness. Optical transparency of glass and quartz permits the dynamics of drying droplets on these substrates to be captured using optical microscopy. Different substrate materials are compared in Table 1 with characterization techniques applied for each of them.

3.2 Surface Chemistry on Designed Substrates

Plasma treated substrates including silicon wafers, quartz slides and glass coverslips were subjected to vapor phase silanization at 70 °C for 24 hours using tridecafluoro-1, 1, 2, 2-tetrahydrooctyl-dimethylchlorosilane. Samples were then submerged in 0.1 wt% PVOH solutions (89-98 kDa and 99+% degree of hydrolysis). Adsorption was allowed to take place at room temperature for 24 hours. Finally, the substrates were labeled with HFBC in the vapor phase at room temperature for another 24 hours. The entire process is illustrated below in Scheme 1.

Scheme 1. Surface modification of silicon wafers with data on thickness increase (ΔT) and advancing/receding water contact angles ($CA=\theta_A/\theta_R$) of the samples after each step.
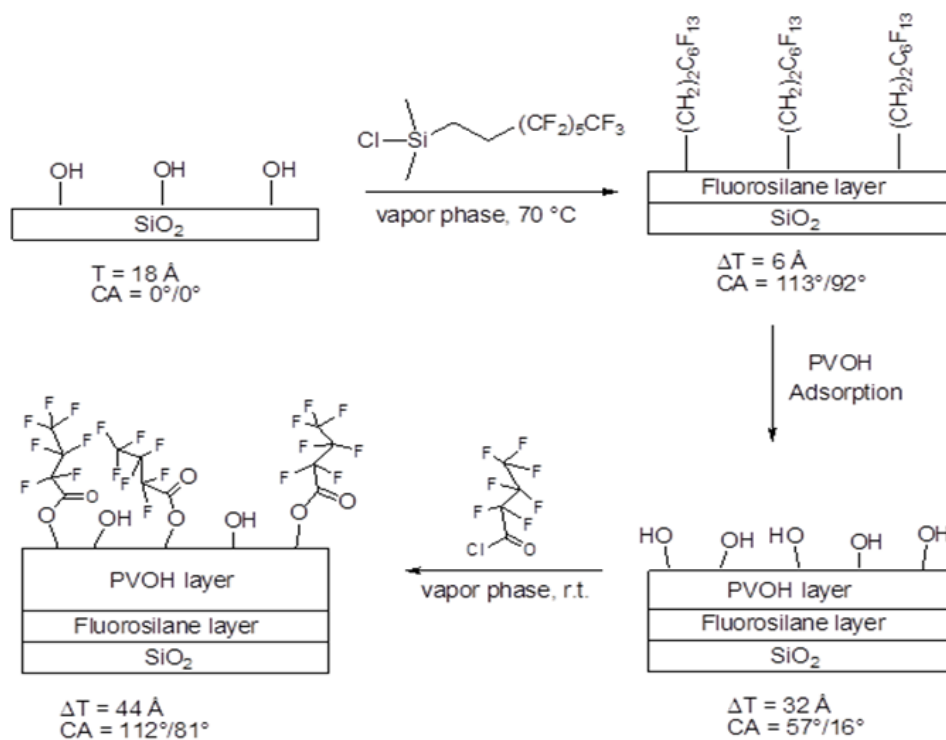
Silicon wafer substrate. Thickness information, contact angle data and

AFM images were acquired after each step of the reaction to assess reaction yield,

surface topography and wettability, as summarized in Appendix 1 (a). Native

silicon wafers after plasma treatment have extremely smooth and hydrophilic

surfaces. Cleaned wafers have a silicon dioxide layer, with average thickness of

18 ± 1 Å and dynamic water contact angles of $0°/0°$. After silanization for 24 hours,

a monolayer of silane molecules was attached uniformly to the substrate as

indicated by the RMS roughness value around 0.2 nm. This step is shown again

below in Scheme 2. Occasionally, unattached silane molecules dimerize and form

aggregates appearing as small dots in AFM images. To avoid this, all samples were agitated vigorously in toluene so unattached silanes on the substrates were shaken off. The smooth and hydrophobic nature of the silane layer is also indicated by its high advancing and receding contact angle values and low hysteresis. Comparing the two images of silanized silicon wafers listed in the appendix, we find that surface wettability as indicated by dynamic contact angle measurements, together with surface roughness, are not sensitive enough to these small aggregates.

Scheme 2. First step of the reaction: silanization on silicon wafers.
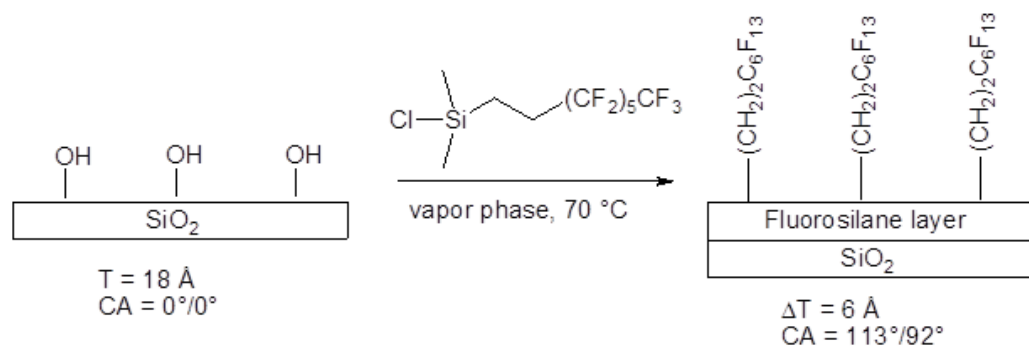
Scheme 3 shows the next step to hydrophilize the substrates. Subsequent PVOH adsorption onto the hydrophobic silane surfaces can form two different surface topographies as shown in Appendix 1(a), depending on the drying rate after samples were rinsed with copious amounts of water. Because of the hydroxyl groups on the polymer side chains, both surfaces exhibit much higher hydrophilicities than the silane substrates. And both have rougher surface topographies after polymer adsorption. A continuous film is formed under slow

and mild drying conditions, which typically gives rise to a RMS value around 0.4

nm; on the other hand, a fast drying rate usually induces water molecules

embedded in the polymer layer to evaporate much faster. The fast water

evaporation is mainly responsible for small holes observed in the polymer film.

Existence of these holes is also indicated as steep depressions in the cross-section

profile, which measures the variations in surface roughness and changes in

thickness. As expected, a continuous film is smoother with more consistent

contact angle values. It was found that on a discontinuous film, probe liquids

sometimes would hop on the substrate, making dynamic contact angle

measurements difficult. Sometimes, the advancing contact angle values spanned

the range of 35° to 50° on the same substrate. While the advancing contact angle

is quite sensitive to different surface features, the receding contact angle doesn't

seem to be greatly influenced in this case. It seems to indicate that PVOH chains

on the surface have rearranged their configurations under different drying rate so

that the hydrophobic domains have undergone changes but the hydrophilic

domains remain uninfluenced. Both types of surfaces were used later as substrates

to study droplet drying dynamics.

Scheme 3. Second step of the reaction: PVOH adsorption on silicon wafers.
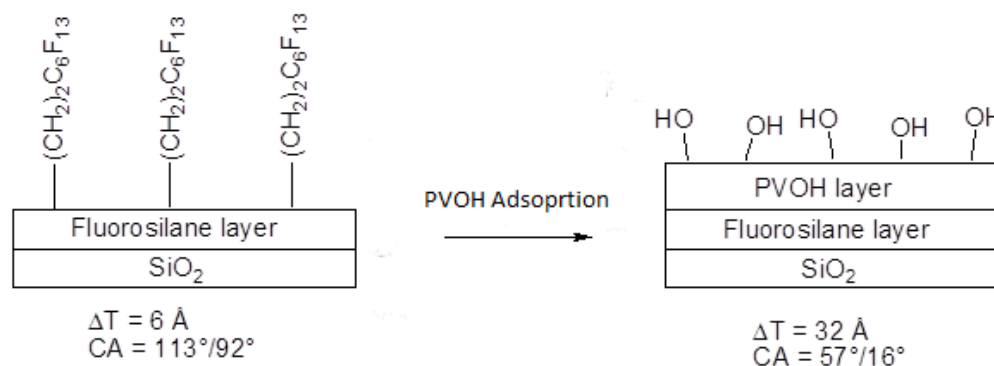
Lastly, HFBC reacts with surface hydroxyl groups for hydrophobization. The reaction is emphasized in Scheme 4. For samples prepared in a tightly sealed environment and rinsed thoroughly afterwards, surface hydrophobicity can reach very high when measured with both pure water and a concentrated (10x) nanoparticle-PVOH solution. The advancing contact angle is as high as that on a silanized surface, while the receding contact angle decreases by more than 10° due to the unreacted hydroxyl groups remaining on the substrate.

Differences between this layer and the silane layer lie in thickness and surface roughness, which is also inferred by the slightly larger contact angle hysteresis. Surfaces labeled with HFBC have a typical roughness of ~0.6 nm. A few deep holes are commonly observed in AFM images for both types of HFBC substrates, implying that these HFBC molecules are able to react with, cover up and even flatten out many of the "bumpy" regions as created previously by PVOH adsorption. As a result, the film swells upon esterification with a little change in surface roughness, regardless of the previous PVOH film topography.

Scheme 4. Last step of the reaction: HFBC labeling on silicon wafers.
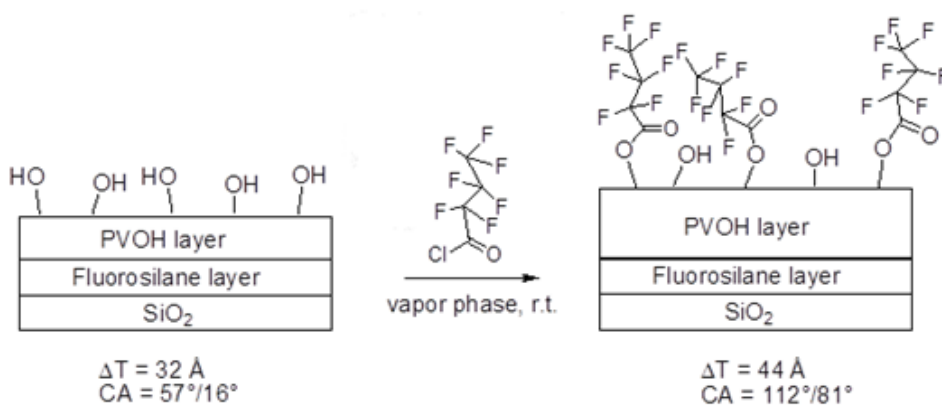
Ellipsometric measurements were employed for estimating the extent of chemical modification of adsorbed PVOH using HFBC on silicon wafers. Since the thickness of the parent PVOH film can vary significantly based on experimental conditions, only data from the continuous film were used. Thickness increase in the PVOH layer contains information about the extent of the reaction with HFBC labeling. For instance, upon reacting a PVOH repeat unit with one HFBC molecule, its molecular weight increases from 44 to 240 g/mol. The newly formed PVOX unit has a density of approximately 1.6 g/cm^3 assuming volumes are additive. Suppose that the lateral dimensions of the film retain constant, this change of volume is directly reflected by the ellipsometric thickness change. Therefore, the ellipsometric thickness can be quantitatively related to the conversion yield of alcohol groups of PVOH in the esterification process:

$$\text{Percent Yield} = \frac{\text{MW}_{\text{PVOH}} \cdot \rho_{\text{PVOX}}(d_{\text{PVOX}} - d_{\text{PVOH}})}{d_{\text{PVOH}}(\rho_{\text{PVOH}} \cdot \text{MW}_{\text{PVOX}} - \rho_{\text{PVOX}} \cdot \text{MW}_{\text{PVOH}})} \times 100\%$$

where MW$_{\text{PVOH}}$ is the formula weight of PVOH repeat unit, -CH$_2$CH(OH)- (44 g/mol);

MW$_{\text{PVOX}}$ is the formula weight of a PVOH derivative (e.g., 240 g/mol in this case);

ρ_{PVOH} is PVOH density (1.3 g/cm^3);

ρ_{PVOX} is the density of PVOX (e.g., 1.6 g/cm^3 in this case);

d_{PVOH} is the ellipsometric thickness of the parent PVOH film (32 Å);

d_{PVOX} is the ellipsometric thickness of the film after modification (76 Å).

The above calculation gives ~ 40% conversion of alcohol groups after HFBC labeling. All other surface characterization data for silicon wafer and quartz, including dynamic contact angle measurements and surface topography, are collected in Appendix 1.

Experimentally, rinsing and drying HFBC labeled substrates can be tricky. Substrates with aggregates or even with donut-shaped "rings" on these surfaces were sometimes obtained. Consequently, these surfaces have much rougher topography. In addition, receding contact angle drops dramatically as roughness increases due to the effect of surface defects, while advancing contact angle stays unchanged. The continuous HFBC labeled film shows a maximum conversion rate of 40% and an even lower conversion rate associated with the discontinuous one is speculated.

On both silane and PVOH surfaces, dynamic contact angles are essentially the same using either pure water or the nanoparticle solution as probing liquids. However, on surfaces labeled with HFBC, the receding contact angle changes significantly when the nanoparticle solution is withdrawn from the solid substrate. It is suspected that when the liquid is withdrawn, the colloidal particles have had time to interact with the surface substantially and are more pinned at the contact line on a rougher suface. As a result, θ_R is lowered. Later it will be pointed out that differences in θ_R suggest different drying mechanisms for pure water and

colloidal sessile droplets. All dynamic contact angle measurements on silicon

wafers are presented in Table 2.

Table 2. Dynamic contact angle data for silicon wafer supporting materials after each step of reaction.

Surface Chemical Species on Silicon Wafers	Water Contact Angle (°) (θ_A/θ_R)	Nanoparticle Solution (°) (θ_A/θ_R)
Plasma Cleaned	0/0	0/0
Silane	113±2/92±2	111±3/90±2
Continuous film of PVOH	57±2/16±2	62±2/16±2
Discontinuous film of PVOH	41±2 /16±2	38±2/17±2
HFBC smooth film	112±2/81±2	111±3/74±2
HFBC rougher film	108±2/75±2	110±5/58±2
HFBC roughest film	109±2/69±4	109±2/54±4

Quartz substrate. Bare silicon wafers and quartz surfaces are so hard and

atomically smooth that once examined under AFM, the tip scratches the surface

and induces surface roughness. However, it can be assumed that depositing a

uniform silane layer on both surfaces does not change the physical roughness of

the original supporting materials. Also notice that due to manufacturing variations,

silanized quartz substrates can have significantly larger roughness values. From

the AFM images, detailed surface textures of bare quartz slides can be observed.

Section analysis profile further discloses information on surface textures, i.e.,

surface waviness. It is obvious that the quartz substrates all have some degree of

curvature, as shown in Figure 9. Not surprisingly, these surface features result in

smaller receding contact angle values and thus larger hysteresis, compared to their counterparts on silicon wafers.

Figure 9. A model showing a bare quartz substrate with surface curvature.[62]

Subsequent adsorption of PVOH molecules again results in two different surface topographies depending on the drying rate. Under a high drying rate, fast water evaporation from the adsorbed layer results in phase segregation and therefore very rough surface topography. Section analysis profile of the height image for continuous POVH films indicates that the substrates still exhibit some curvature (see Appendix 16).

The final step of HFBC labeling on quartz substrates flattens out the previous layer to a surprising extent that the original curvature is almost completely covered, as depicted in the section analysis profiles. Similar to that of HFBC labeled silicon wafer substrates, receding contact angle on quartz substrates decreases as the surface gets rougher, and it is further lowered when colloidal droplet is used to probe the surface. These data are summarized below in Table 3.

Table 3. Dynamic contact angle data for quartz supporting materials after each step of reaction.
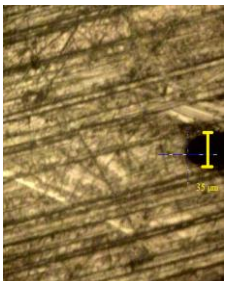
Surface Chemical Species on Silicon Wafers	Water Contact Angle (°) (θ_A/θ_R)	Nanoparticle Solution (°) (θ_A/θ_R)
Plasma Cleaned	0/0	0/0
Silane	110±2/77±2	110±2/75±2
Continuous film of PVOH	61±2/14±2	61±4/14±2
Discontinuous film of PVOH	41±2 /16 ±2	36±2/8±2
HFBC smooth film	111±2/80±2	110±2/74±2
HFBC rough film	109±4/72±2	107±2/64±2

Glass substrate. Glass substrates are too rough to be characterized using AFM. Therefore, only contact angle values were recorded (Table 4). A macroscopic image was included to show surface topography of a typical silanized glass slide. To show scale, a ~35 μm wide AFM cantilever was included in the image. It can be seen that the glass substrate is very rough. Due to crude cutting and polishing in manufacturing, the substrates are left with many surface defects such as grooves. To our surprise, the silanized glass substrate exhibits a slightly higher θ_R than that of a quartz slide. It is speculated that the texture of the substrates may contribute to substrate receding contact angle. It is also possible that surface OH group density of the original substrate is correlated to the dynamic receding contact angle. Silicon wafer has the highest OH group density on its surface so silanization gives the most uniform layer as compared to silanization on quartz substrate, which has the lowest OH group density. The uniform layer is numerically represented as having low hysteresis. In this case,

glass substrate has medium OH group density and thus medium hysteresis. Further surface modification with PVOH adsorption and HFBC labeling may have covered up this feature. Consequently, these chemically modified glass substrates display similar wettabilities as silicon wafers and quartz substrates.

Table 4. Dynamic contact angle data for glass supporting materials after each step of reaction.

Surface Chemical Species on Glass Substrates	Water Contact Angle (°) (θ_A/θ_R)	Nanoparticle Solution (°) (θ_A/θ_R)	Macroscopic Image of A Silanized Glass
Plasma Cleaned	0/0	0/0	
Silane	109±2/85±2	106±2/81±2	
Continuous film of PVOH	61±2/14±2	60±2/13±2	
Discontinuous film of PVOH	41±2 /14±3	38±2/14±2	
HFBC	109±2/79±2	110±2/75±2	

3.3 Characterization of Components in the Liquid Phase

We chose to work with two grades of PVOH polymers: one with MW of 13~23 kDa and degree of hydrolysis of 98% and the other one with MW of 89-98 kDa and degree of hydrolysis of 99+%. Both samples are almost completely hydrolyzed so that the role of unhydrolyzed poly(vinyl acetate) segments is negligible during adsorption onto surfaces of gold nanoparticles and/or upon further interactions with various substrates.

For PVOH with degree of hydrolysis greater than 90%, complete dissolution is attained in hot to boiling water while partially hydrolyzed species

(less than 90% hydrolyzed samples) are soluble at room temperature with mild

stirring. Highly hydrolyzed PVOH samples have more hydroxyl groups,

contributing to strong hydrogen bonding both intra- and intermolecularly. These

interactions are so predominant that solubility in water is reduced as the result. On

the contrary, partly hydrolyzed samples have residual acetate groups weakening

intramolecular hydrogen bonding and are thus readily dissolved under ambient

conditions. Once dissolved, these sample solutions are able to stay kinetically

stable up to 3 months.

Dissolved polymers show good monodispersity as indicated by the

polydispersity index (PDI) value in DLS measurements. This value measures size

distribution in a given polymer sample. For example, if the polymer chains

approach uniform chain length, the PDI approaches zero. Using a 0.04 wt%

citrate solution, highly monodisperse colloidal gold was synthesized successfully

and characterized by both DLS and Transmission Electron Microscopy (TEM).

The TEM image in Figure 10 displays the gold nanoparticles cast on a carbon-

coated TEM grid. These nanoparticles have an average diameter of ~15 nm

measured via TEM, slightly less than their hydrodynamic diameter of ~22 nm,

characterized by DLS. By decreasing the amount of the reducing agent, larger

sizes of gold nanoparticles have also been prepared. However, these colloids were

found to be unstable overtime due to particle aggregation. In addition, smaller

particles with a diameter of less than 10 nm are not able to precipitate during

centrifugation. Therefore, gold nanoparticles of 15 nm in diameter are the most feasible to work with.
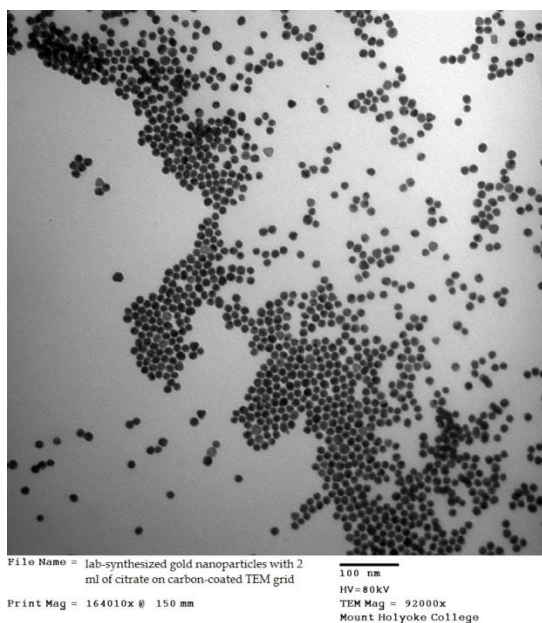
Figure 10. A TEM image of gold nanoparticles synthesized by the citrate reduction method. The average diameter is measured to be 15 nm.

Previous studies indicate that PVOH of 13~23 kDa is able to form closely packed complexes with gold nanoparticles as well as to provide sufficient steric hindrance to prevent particle aggregation. Localized surface plasmon resonance of individual AuNPs gives rise to their intense red color.[34] Closely packed AuNPs absorb light at longer wavelengths, the extent of which depends on the interparticle distance and aggregation state.[63] Figure 11 displays that spectroscopic peak shifts as the adsorption of PVOH onto nanoparticle surfaces changes interparticle distance in solution. In the solid deposit patterns, the blue region of the deposit is more red-shifted than the purple deposit due to closely

packed and/or aggregated particles. Therefore, color and intensity of a dried

sessile drop containing AuNPs allow us to draw some conclusions about particle

distribution and uniformity of interparticle distance across the deposit.
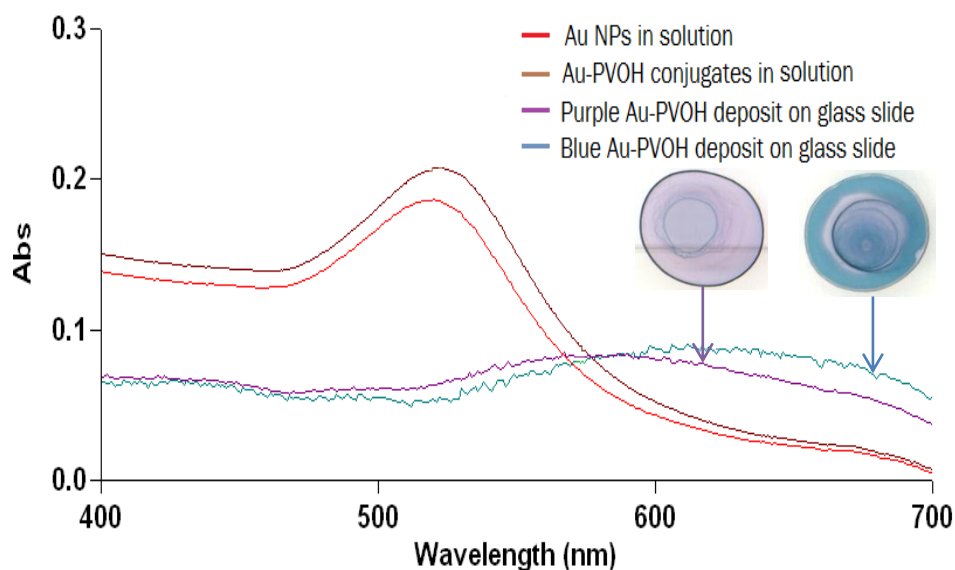
Figure 11. Spectroscopic peak shifts indicate a distinction in optical properties between colloidal AuNPs and self-assembled AuNPs from aqueous sessile droplet. Spherical shaped AuNPs were synthesized by citrate-reduction and are 15 nm in diameter. AuNPs were complexed with commercially available poly(vinyl alcohol) with MW of 13~23k and degree of hydrolysis of 98%. Solid deposits shift more to the longer wavelength depending on the extent of particle aggregation.

A different molecular weight polymer, PVOH of 89~98 kDa, was used to

construct a more hydrophilic layer on top of the hydrophobic silane layer. When

deposited on the silane layer, the polymer chains crystallize by folding back and

forth many times. A domain of stacks of these folded chains is called a lamellae

(Figure 12).[64] Irregular polymer chains meander in and out of ordered crystalline

portions. The crystalline portion is in the lamellae and the amorphous portion is

outside of the lamellae. Polymers with relatively short chains may only fold

partially on themselves, leaving behind many "tails" wander outside of the

crystalline lamellae. As a result, these polymer surfaces are not uniform and are

difficult to control. On the other hand, intermediate polymer chain length as the

one used here (89~98 kDa) is more favorable in the formation of a smooth and

continuous film. A more detailed characterization has been reported in the

previous session.
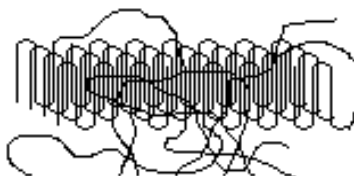
Figure 12. A stack of polymer chains folded back on themselves is called a lamella. Some chains can stay outside the lamella in the amorphous region.[64]

Table 5 summarizes DLS measurements for various components in

solution. Hydrodynamic diameter offers information on the average size of each

component assuming spherical shape. The more important piece of information

lies in the PDI value, an indication of the monodispersity of the species in

solution. From the table, all species exhibit high monodispersity before being cast

onto a solid substrate.

Table 5. DLS size measurements of PVOH, colloidal gold and their conjugates.

Chemical Species	Hydrodynamic Diameter	PDI
Au nanoparticle	23.3nm	0.163
PVOH chain (13~23 kDa; 98% hydrolyzed)	8.4 nm	0.395
PVOH chain (89~98 kDa; 99+% hydrolyzed)	22.2 nm	0.124
Au-PVOH (13~23 kDa) complex	49.6 nm	0.161

3.4 Drying Process of Sessile Droplets on Previously Designed Solid Substrates

In this session, experimental results concerning the evaporation of both colloidal and pure water droplets on substrates with different extents of hydrophobicity and surface roughness are presented. The main results show the evolutions of the contact diameter as well as the contact angle of the droplets during evaporation.

Plasma cleaned hydrophilic substrates. All substrates are superhydrophilic after plasma treatment, as demonstrated by the vanishing dynamic contact angle values. Liquids can easily spread on hydrophilic surfaces; a small volume can often take up a large contact area at the beginning of droplet evaporation. The drying process and final deposit pattern are similar on glass and quartz slides: once deposited, the droplet spreads out and wets the substrate completely. Contact line is slightly pinned by the nanoparticles at the periphery. The receding contact line then moves steadily inward. Due to small contact angle hysteresis and slow contact line movement, the drying front leaves uniformly distributed nanoparticles behind on the substrate (Figure 13, left). Towards the end of the drying process,

drying rate speeds up and nanoparticles suspended in the liquid are highly concentrated because of solvent evaporation. Therefore, these particles tend to form aggregates, as presented by the bluish region in Figure 13 (right). For a pure water droplet, only contact line retraction upon evaporation was observed.
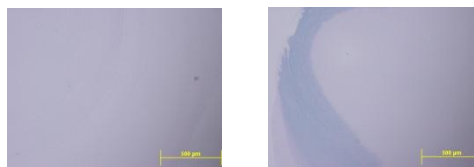
Figure 13. Left: Particles deposited at the periphery of the deposit; Right: Particles deposited in the central region of the deposit.

Silanized hydrophobic substrates. The evolution of the observed contact angle, θ, versus time, t, for pure water and colloidal droplets on silanized substrates is presented in Appendix 2 (left column). On silicon wafer and quartz supporting materials, both liquids exhibit similar behaviors in contact angle evolution: there is a continuous decrease in static contact angle during the first short stage of the evaporation, followed by a plateau region for about 50% of the remaining droplet lifetime. At the very end, a rapid decrease in the contact angle is observed. On glass, the contact angle decreases monotonically during the evaporation of colloidal droplet, which is due to the pinning of the contact line. In contrast, pure water on glass remains fairly constant contact angle after an initial decline. The pattern resembles the previous two substrates.

In terms of the contact diameter, *D*, presented in Appendix 2 (right column), two distinguishable behaviors of the contact line are noted. Since silicon wafers are not optically transparent, the evolutions of contact diameters based on optical images were only obtained on quartz and glass substrates. In general, diameter of every droplet was measured four times at different locations using ImageJ. The average value was plotted against time, with the standard deviation represented by the error bar; a large error bar indicates a distorted (usually oval) shape of the deposit. On quartz substrates with a uniform silane layer, there is virtually a monotonic receding of the base diameter at constant rate for at least half of the droplet lifetime, followed by more rapid receding until evaporation is complete. Typically, the contact diameter changes very little at the initial stage of drying. It seems that at the time when the contact diameter starts to decline linearly, there is a corresponding drop in the contact angle after which the contact angle remains stabilized. In this case, the contact angle is stabilized at ~80°, close to the receding contact angle of the surface. Pure water and colloidal droplets behave very similarly. Together with the evolution of contact angle, we can describe the entire drying process on a silanized quartz slide: a droplet sitting on the substrate maintains its initial contact area while the contact angle decreases. When it reaches the receding contact angle, the contact area starts to decrease (contact line depinning) while maintaining its contact angle at θ_R. At the end, the colloidal droplet is pinned due to the deposition of concentrated nanoparticles in the liquid phase and contact angle drops abruptly. In contrast, the water droplet

shrinks at a higher rate towards the end, with a simultaneously decreasing contact angle. From the magnitude of error bars, we can also conclude that both liquids maintain circular shapes during the entire evaporation processes.

The other type of contact line evolution is presented by the red line on silanized glass substrates. Pinning of the contact line is observed during most the droplet lifetime as indicated by the constant contact diameter, followed by a continuous and later interrupted decrease. Drying starts with a constant contact area and decreasing contact angle, same as the previous case. When contact angle decreases to θ_R, particles at the drying front deposit and pin the contact line. The large standard deviation associated with a decreasing contact diameter near the end of evaporation suggests a slip of the contact line and partial pinning. At this stage, the shape of the contact line becomes more elliptical than circular.

Interestingly, contact line depinning of a colloidal droplet was observed on a silanized glass substrate, as illustrated by the yellow line on the same plot. Although a corresponding plot of contact angle evolution is not available, similar drying process as that on a silanized quartz slide can be predicted. The behavior of a sessile water droplet remains the same on both substrates.

PVOH-adsorbed hydrophilic substrates. Due to surface hydrophilicity, droplets take up relatively large footprint upon deposition. In order to record the entire droplet profile within the viewing window of an optical microscope, casting volume is adjusted accordingly (see Appendix 3). In addition, the actual casting

volume can deviate quite a bit due to experimental limitations. Therefore, the discussion is qualitative, based on the general trend of contact angle and contact diameter variations during droplet evaporation.

After PVOH adsorption, two surface topographies based on different drying processes, continuous and discontinuous films, were typically obtained. From the evolution of the contact angle, θ, versus time, t, as presented in Appendix 3 (left column), similar patterns were observed on these two films. It seems that the discontinuous PVOH film is only different in its initial contact angle. On every type of substrate, with continuous or discontinuous PVOH coverage, contact angle for an evaporating colloidal droplet decreases monotonically; while for a water droplet, a steady decrease in contact angle is noticed for at least half of the droplet drying lifetime, followed by a short plateau around the dynamic receding contact angle.

Together with the evolution of the contact diameter, D, versus time, t, (Appendix 3, right column), the whole drying process on PVOH substrates can be described as the following. On a quartz slide, contact angle decreases steadily while contact line stays pinned for a colloidal droplet. Then the drying front starts to move inward while contact angle keeps decreasing until the end. It seems that a droplet sitting on a discontinuous film assumes more elliptical shape during evaporation caused by chemical "defects", compared to droplets drying on more continuous films. This is implied by the larger magnitude of its error bars. A

sessile water droplet dries quite differently from a droplet containing

nanoparticles. The water droplet remains its contact area until towards the very

end. At this point, the contact line retracts very fast but the contact angle is

stabilized around its dynamic receding contact angle (~15°). This fits in a typical

contact line depinning model and it proves strongly that contact line depins when

the contact angle reaches its dynamic receding contact angle.

Drying processes on glass substrates are very similar to those on quartz

substrates. Water and colloidal solution dry via two different mechanisms. On

glass substrates, it seems that overall, droplets assume elliptical shapes during

evaporation on either continuous or discontinuous film, caused by chemical

and/or physical defects.

HFBC-labeled hydrophobic substrates. HFBC labeled silicon wafers can

exhibit quite different surface topographies as listed in Appendix 1. Not

surprisingly, the evolution of the contact angle plots (Appendix 4, left column)

show two different drying trends for sessile droplets containing nanoparticles. For

smooth and slightly rougher surfaces, contact angle declines steadily until it

reaches and stabilizes around θ_R. On a very rough surface, however, it is observed

that contact angle keeps decreasing until the end. On the other hand, pure water

droplets always have contact angle stabilized around θ_R, which is slightly higher

than θ_R for colloids. This observation corresponds nicely with the dynamic

contact angle measurements using water and colloids as probe liquids, as reported

in Appendix 1.In short, colloidal droplets are not pinned on smooth surfaces but pinned on rough surfaces.

HFBC labeled quartz substrates can have very similar surface topography as that on silicon wafer supporting materials, likely because this last step of surface modification can cover up the physical roughness of the original substrates. Combined with the evolution of the contact diameter plots (Appendix 4, right column), contact line appears to be depinned on a continuous film, as water and colloidal solution retract almost at the same time. On a discontinuous film, contact diameter of a colloidal droplet remains the same well after water starts to retract, indicating contact line pinning mechanism. Colloidal solution depositing on HFBC modified glass slides shows the same contact line pinning behavior. On all substrates labeled with HFBC, a water droplet depins around its θ_R, regardless of surface topography or composition.

3.5 Explanation of Drying Dynamics Based on Experimental Observations

The aim of this section is twofold. On one hand, the effects of surface physical and chemical characteristics on the kinetics of the three-phase contact line of evaporating droplets containing concentrated nanoparticles are explored. At the same time, the effect of the nanoparticles on the pinning-depinning phenomenon is investigated via a comparison to the evaporation processes of pure water droplets.

In short, on a perfectly smooth, chemically homogeneous, and hydrophilic surface, coffee-ring effect is eliminated from the edge of the final deposit. The complete wetting results in a large contact area and a relatively thin film of droplet. The evaporation rate at the edge is not much faster then that at the center. The particles moving to the edge still end up depositing, but the driving force induced by concentration gradient is much weaker in this case. As the result, a uniform distribution of particles is left behind as the drying front moves inward slowly. Aggregates are formed at the later stage of drying due to increased concentration of the colloids. The vanishing hysteresis guarantees only slight pinning at the droplet edge. Due to the absence of particles, pure water droplet does not experience contact line pinning upon drying.

Being both physically smooth and chemically homogeneous, silanized silicon wafers have hydrophobic surfaces and low hysteresis. Small aggregates remaining on the surface don't influence these properties much. Therefore, during droplet evaporation, the evolution profile is similar to the behavior expected on ideal hydrophobic surfaces, with a constant contact angle and decreasing contact area.

Silanized quartz slides are chemically homogeneous but physically slightly rougher. Hysteresis is a qualitative tool to reflect the joint-effect of these surface properties. In this case, both lower surface OH group density and the wavy nature of the substrate contribute to the larger hysteresis. Surface roughness

also comes mainly from the surface textures. On such surfaces, contact angle may not be as stabilized as on silanized wafer substrates during droplet retraction, but the behavior of an evaporating droplet, in general, resembles ideality. It seems that the slight physical roughness doesn't exert enough force in contact line pinning; and surface chemical homogeneity guarantees uniform retraction of the contact line. Drying mechanism for pure water and colloidal droplets is similar except toward the end, where the latter experiences contact line pinning due to the deposition of concentrated nanoparticles.

Droplets on silanized glass substrates can exhibit quite different drying mechanisms, with completely pinned, partially pinned or depinned contact line. Appendix 2 shows partial pinning (red line) and depinning (yellow and blue lines). Contributing factors for these different drying behaviors are very difficult to identify as glass substrates are characterized only by dynamic contact angles. Considering its very rough surface, silanized glass substrate exhibits surprisingly low hysteresis (lower than that of a quartz slide). As mentioned earlier, hysteresis takes into account of many surface properties. It is doubtful that the value here correctly predicts surface physical roughness. As 90% of our colloidal samples partially or completely pinned on glass substrates, it seems the physical roughness has applied a stronger force in contact line pinning as opposed to the depinning force, exerted by the hydrophobic and homogeneous chemical species on the surface. As a result, the colloidal solution is dried with a constant contact area and decreasing contact angle, as if the substrate is hydrophilic.

Due to the absence of particles in the droplet, the contact line of a pure water droplet is not pinned on rough glass substrates. The surface silane molecules interact only weakly with water molecules. The small adhesive forces between the solid and the liquid, and the stronger cohesive forces within the liquid cause contact line retraction.

HFBC labeled substrates serve as great comparisons to silanized substrates since both are hydrophobic. In general, HFBC substrates are chemically heterogeneous, given the low surface OH group conversion percentage. Surface unreacted OH groups, PVOH hydrophobic backbone together with HFBC modified domains all contribute to chemical heterogeneity and lowered θ_R. In addition, the wavy nature of quartz slide disappears after this last step of surface modification so the effect of physical roughness on droplet evaporation is minimized. To our surprise, the depinning behavior of a colloidal droplet on glass seems to also imply a greatly "smoothened" surface. In short, these HFBC labeled hydrophobic substrates are physically smooth, but chemically rough to various extents.

The formation of continuous HFBC films on either silicon wafers or quartz slides gives low RMS roughness of 0.6 nm. The chemical "roughness," however, may induce complex solute-substrate interactions locally, holding the drying front. During that time, contact angle keeps decreasing to θ_R value.

Contact line depins afterwards because this pinning force is no longer strong enough.

The formation of holes and thus discontinuous HFBC films gives larger surface roughness (RMS on wafer substrate = 3.3 nm; RMS on quartz = 1.1 nm). At this point, the surface can exert a larger pinning force caused by the high chemical heterogeneity. Therefore, contact line of an evaporating colloidal droplet is pinned for most of the droplet lifetime. The universally observed depinning behavior of water droplets indicates extra pinning interactions between solute particles and the substrate that are absent in the case of pure water. This will be discussed further in the next section.

Drying on hydrophilic PVOH-modified surfaces is considered next. On a silicon wafer substrate, the formation of discontinuous film after PVOH adsorption makes the surface chemically more heterogeneous. This results in a slightly rougher surface topography (RMS = 0.4 nm) and more hydrophilic characteristic. On a quartz slide, the wavy nature of the substrate adds surface physical roughness to both continuous films (RMS = 0.7 nm) and discontinuous films (RMS = 2.1 nm). Although detailed surface features of glass slides are unknown, dynamic contact angle measurements indicate similar surface wettability compared to other supporting materials.

Because of the hydrophilic characters of PVOH on all types of substrates, colloidal solutions have essentially the same drying mechanisms. Due to the

strong hydrogen-bonding interactions between surface PVOH molecules and PVOH-adsorbed particles, contact line pinning is universally observed before the drying front retracts. The effect dominates over other factors such as physical roughness or chemical heterogeneity in causing contact line pinning. Therefore, similar drying behaviors were observed on all three substrates . Notice that colloids are commonly pinned on hydrophilic surfaces, but water is not. Though the contact area of a water droplet stays constant for ~70% of its lifetime, it also takes roughly the same amount of time for its static contact angle to reach its receding contact angle. And once it reaches the receding contact angle, the contact line recedes quickly and contact area drops dramatically. In the next session, the role of nanoparticles in contact line pinning is discussed using a semi-quantitative method.

3.6 Explanation of Drying Dynamics through Extending Young's Equation

The aim of this section is to provide a more theoretical understanding for contact line pinning and depinning processes reported in the previous section. Young's equation has been used and modified in literature to help elucidating mechanisms of contact line behavior during the evaporation of a droplet. Here, we first present theories developed by other research groups before developing the theories further based on our experimental results. In particular, we hope to emphasize the contribution of the solid substrate and surface chemistry in controlling contact line behavior.

Figure 14 represents the region near the drying front, at equilibrium with contact angle θ_0 and at a slightly smaller angle, θ_0- $\delta\theta$, after some evaporation, assuming contact line pinning.[23] On an ideal substrate, the net force at the three-phase boundary at equilibrium should be zero based on Young's equation (see Figure 4),[22]

$$\gamma cos\theta_0 + \gamma_{SL} - \gamma_{SG} = 0$$

If there is a slight decrease in the angle by $\delta\theta$, a net force results toward the bulk liquid in the magnitude of δF:

$$\delta F = \gamma cos(\theta_0 - \delta\theta) - \gamma cos\theta_0 \approx \gamma sin\theta_0 \delta\theta$$

An intrinsic energy barrier, U, was proposed to counteract this force and thus prevent contact line motion.[23-25] In general, the derivative of this energy with respect to position, $\frac{\partial U}{\partial r}$, represents a pinning force locally opposing depinning, whereas δF attempts to depin the contact line. At the threshold of pinning-depinning, it is established that

$$\frac{\partial U}{\partial r} = \delta F = \gamma sin\theta_0 \delta\theta$$
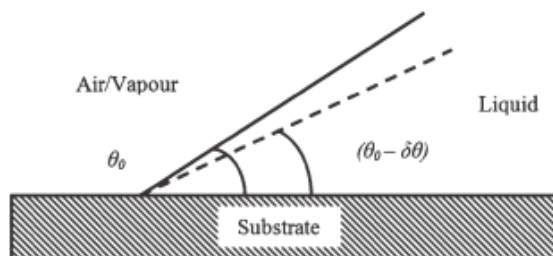
Figure 14. Schematic representation of the contact line region with the liquid at the equilibrium contact angle, θ_0, and a slightly smaller angle, $(\theta_0$-$\delta\theta)$.[23]

As soon as evaporation starts, the decreasing contact angle induces a force, $\delta \boldsymbol{F}$, to contract the droplet. Depinning occurs when either θ_0 or $\delta \theta$ is sufficiently large to supply enough $\delta \boldsymbol{F}$ to overcome the intrinsic energy barrier preventing contact line movement. This depinning force, $\delta \boldsymbol{F}$, is related to the initial contact angle (θ_0), the surface tension of the liquid (water or nanoparticle solution) (γ) and the change in contact angle ($\delta \theta$). Assuming a given pinning force or constant energy barrier, $\frac{\partial U}{\partial r}$, for contact line movement, depinning of the contact line is attained for large initial contact angles because $\gamma sin\theta_0$ is large.[23] On an ideal hydrophobic substrate, such as a silanized silicon wafer, continuous motion of the contact line is anticipated because a very small value of $\delta \theta$ can induce movement. However, for an energy barrier of the same magnitude, when $\gamma sin\theta_0$ is smaller, $\delta \theta$ needs to be significantly large to overcome the energy barrier. For example, on a hydrophilic substrate, such as the one covered with PVOH molecules, an intermediate value for θ_0 is presented. Depinning of pure water doesn't take place until $\delta \theta$ grows large enough to overcome the barrier. Based on our experimental data, the initial movement of the contact line occurs when

$$\delta \theta \approx \theta_0 - \theta_R$$

on hydrophilic surfaces.

It becomes more complicated when the substrate is not ideal (physically smooth and chemically homogeneous). A general term, U_{total}, is used to express the intrinsic energy barrier for the depinning force to overcome in order to induce

contact line movement. Here we would like to propose the different components that the critical energy barrier consists of, U_{pr}, U_{ch} and U_{p-s}. U_{pr} is the potential energy barrier created by surface physical roughness. Due to manufacturing defects, the original supporting materials may exhibit different surface textures: wavy in the case of quartz slides or "groovy" in the case of glass slides. These surface features can produce a pinning force when interacting with a sessile droplet. U_{ch} is the potential energy barrier created by surface chemical heterogeneity. Due to experimental limitations and incomplete chemical conversions, there may be several chemical species (including aggregates and dust particles) present on the surface. When exposed to an evaporating liquid, the high surface energy components pin the liquid drying front. Lastly, U_{p-s} is the energy barrier created by interactions between particles in the liquid and the substrate. In addition, the particles accumulated at the contact line further pin the contact line. As a result, U_{p-s} builds up quickly at the contact line, and depinning becomes progressively more difficult. Later it will be illustrated that this quantity is positively proportional to parameters representing surface physical and chemical features. All in all, the totally energy barrier can be written as

$$U_{total} = U_{pr} + U_{ch} + U_{p-s}$$

We can imagine that on an ideal and hydrophobic substrate, depinning force is big due to a large initial contact angle. Furthermore, U_{total} is minimized because all three components are negligible. Consequently, pinning force is very weak and a small change in contact angle ($\delta\theta$) can induce contact line movement

immediately. This is best illustrated in the case of silanized wafer, which has the most stabilized contact angle evolution around its θ_R. The superimposed water and colloids contact angle evolution trends imply little particle-substrate interactions for a sessile colloidal droplet on the hydrophobic silane layer. As discussed above, adhesive forces between the liquid droplet and the hydrophobic substrate is very small. Cohesive forces within the liquid cause the drop to ball up and minimize interactions with the surface.

A silanized quartz substrate is physically rougher and thus has a non-zero U_{pr}. The increased U_{total} holds the drying front until the depinning force accrues to overcome the energy barrier (when static contact angle reaches θ_R). However, towards the very end, particles in the colloidal droplet have to settle down due to gravity. As they accumulate at the drying front, U_{p-s} soars and the contact line is pinned (called the p-s effect). Due to the absence of particles in pure water, contact line keeps receding until the evaporation is complete. Therefore, the term U_{p-s} is trivial for both pure water and colloids until the very end of the drying process. The silanized quartz substrates have best illustrated this. On a silanized glass, U_{pr} dominates over other terms and the p-s effect occurs again. As a result, contact line is mostly pinned throughout for colloidal solutions.

Comparatively, HFBC labeled silicon wafers have a bigger U_{ch} (compared to silanized ones) that promotes contact line pinning. As a result, $\delta\theta$ has to grow to a significant magnitude before the contact line depins. Normally, this number

is the difference between θ_0 and θ_R. However, if U_{ch} is too large to be surmounted by a change in contact angle, then the contact line is pinned and contact angle is further lowered (See Appendix 4 as a reference). If this were the complete story, essentially the same behavior for water would be observed. Notice that the existence of either U_{ch} or U_{pr} promotes particle-substrate interactions and thus produce a bigger U_{p-s} than when U_{ch} and U_{pr} are negligible, since particles interact favorably with surface defects. We believe that it is this rising U_{p-s} differentiating the behavior of an evaporating water droplet from that of a colloidal droplet.

Silanized quartz slides and HFBC labeled quartz slides (continuous) have contributing U_{pr} or U_{ch} that can potentially pin the contact line. It seems that a larger U_{p-s} is induced on the discontinuous film due to a larger U_{ch} and contact line pinning occurs for colloidal solutions. Silanized and HFBC labeled glass substrates follow the same train of reasoning.

On an ideal and hydrophilic substrate (e.g. plasma cleaned quartz substrate), θ_0 is small and U_{p-s} is the contributing factor to pinning. A small depinning force and a relatively large pinning force are expected. Due to a large contact area, however, only a few particles actually reach to the drying front and thus contact line is only vaguely pinned. After hydrophilizing the substrates with PVOH adsorption, all three components U_{pr}, U_{ch} and U_{p-s} contribute significantly in contact pinning. The hydrogen bonding interactions between

solute particles and the surface molecules are very strong. The existence of U_{ch} and/or U_{pr} intensifies these interactions so that all colloidal droplets have contact line pinned on the hydrophilic substrates.

Intuitively, we can see that $U_{\text{p}-\text{s}}$ is related to both U_{pr} and U_{ch} but the exact relationship remains unknown. At this stage, our discussion is mostly qualitative. Future studies focusing on quantifying these surface parameters are critical in developing a thorough understanding of the wetting and drying phenomena. They will also help to predict the droplet drying behaviors and to design surfaces accordingly to give desirable deposit patterns.

4. CONCLUSIONS AND FUTURE WORK

Based on our hypothesis, the total intrinsic energy barrier for contact line pinning consists of three components: U_{pr}, U_{ch} and U_{p-s} , created by substrate physical roughness, chemical heterogeneity and particle-substrate interactions, respectively. These are the contributing factors in producing a pinning force at the three-phase boundary. Meanwhile, a depinning force is found to be proportional to the liquid-gas interfacial tension, γ, sine of the initial contact angle, $\sin \theta_0$ and the change of this contact angle after some evaporation, $\delta\theta$.

To control the pinning force, we adjusted the three energy barrier components. Substrates of distinct physical roughnesses, silicon wafer, quartz and glass, were chosen to tune U_{pr}; U_{ch} is controlled through adjusting surface chemical compositions; U_{p-s} is directly controlled by using sessile droplets with and without nanoparticles. To control the depinning force, we adjusted θ_0 and $\delta\theta$ through surface chemistry. It is further proposed in this study that contact line starts depinning when the static contact angle reaches θ_R, the critical dynamic receding contact angle.

Our experimental data are mostly consistent with the hypothesis: hydrophilic substrates pin the contact line of a sessile colloidal droplet readily because the strong particle-substrate interactions create a huge U_{p-s}. In general, with a small initial contact angle, θ_0, the droplet static contact angle decreases monotonically until θ_R. At this point, the behavior of pure water and colloidal

solution diverges. Pure water droplet stays at θ_R for a while with contact line depinning; however, colloidal solution has contact line pinned with continuous contact angle decline. This implies that as particles accumulate at the drying front, the particle-substrate interactions are intensified, resulting in an even bigger $U_{\mathrm{p-s}}$. Therefore, colloids are pinned while water is not.

Due to a large initial contact angle, θ_0, hydrophobic silane substrates normally don't pin the contact line of a sessile droplet, unless the surface roughness is exceedingly high, as in the case of glass substrates. Different extent of chemical heterogeneity is achieved on HFBC labeled substrates and U_{ch} seems to also contribute to pinning when it gets large enough.

The most notable feature of this study is the lack of coffee ring on the fluorosilane monolayer-supported on quartz. A great progress has been made in understanding the role of various factors in affecting contact line pinning and depinning processes. However, characterization of the surface chemical heterogeneity should be carried out in more details. In the future, silanization to various extents on these substrates will be carried out to achieve high advancing contact angle ($>110°$) and low receding contact angle ($<30°$) simultaneously on one substrate. This will further illustrate the roles of surface chemical heterogeneity and receding contact angle on contact line behavior. In addition, it has been noted that $U_{\mathrm{p-s}}$ is closely related to surface roughness and chemical

heterogeneity. An investigation of the interrelationship among these three terms

will also be carried out.
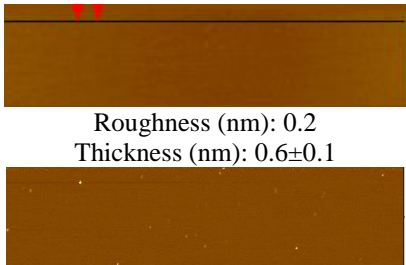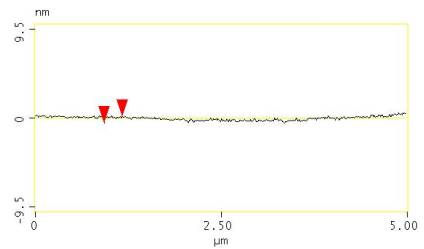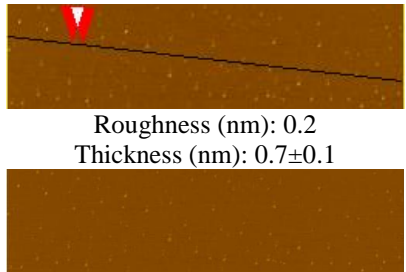
REFERENCES CITED
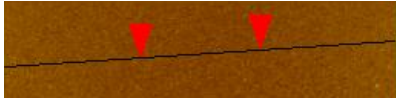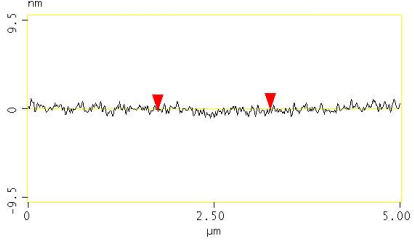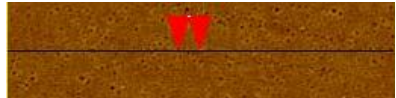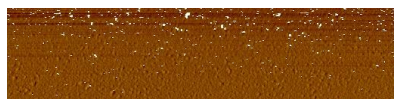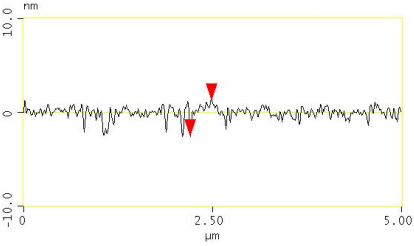
1. Deegan, R. D.; Bakajin, O.; Dupont, T. F.; Huber, G.; Nagel, S. R.; Witten, T. A. *Nature* **1997**, *389*, 827-829.
2. Parisse, F.; Allain, C., *J. Phys II* **1996**, *6*, 1111-1119.
3. El Bediwi, A.B., Kulnis, W.J., Luo, Y., Woodland, D., Unertl, W. N., *Mat. Res. Soc. Symp. Proc*. **1995**, *372*, 277-282.
4. Kuncicky, D. M., Velev, O. D. *Langmuir* **2008**, *24,* 1371-1380.
5. Deegan, R. D.; Bakajin, O.; Dupont, T. F.; Huber, G.; Nagel, S. R.; Witten, T. A. *Phys. Rev. E* **2000**, *62*, 756-765.
6. Deegan, R. D. *Phys. Rev. E* **2000**, *61*, 475-485.
7. Hu, H.; Larson, R. G. *J. Phys. Chem. B* **2006**, *110,* 7090-7094.
8. Park, J.; Moon, J. ; *Langmuir* **2006**, *22,* 3506-3513.
9. Takhistov, P.; Chang, H. –C. *Ind, Eng. Chem.Res.* **2002**, *41*, 6256-6269
10. Hong, S. W.; Giri, S.; Lin, V. S.-Y.; Lin, Z. Q. *Chem. Mater.* **2006**, *18*, 5164-5166.
11. Lin, Y.; Balizan, E.; Lee, L. A.; Niu, Z. W.; Wang, Q. *Angew. Chem. Int. Ed.* **2010**, *49*, 868-872.
12. Lin, Y.; Su, Z. H.; Xiao, G. H.; Balizan, E.; Kaur, G.; Niu, Z. W.; Qiang, W. *Langmuir* **2011**, *27*, 1398–1402.
13. Tan, K. W.; Koh, Y. K.; Chiang, Y. M.; Wong, C. C. *Langmuir* **2010**, *26,* 7093-7100.
14. Bhardwaj, R.; Fang, X. H.;, Somasundaran, P.; Attinger, D. *Langmuir* **2010**, *26,* 7833-7842.
15. Zhang, Y.; Yang, S.; Chen, L.; Evans, J. R. G. *Langmuir* **2008**, *24,* 3752-3758.
16. Monteux, C.; Lequeux, F. *Langmuir* **2011**, *27*, 2917-2922.
17. Yunker, J. P.; Still, T.; Lohr, A. M.; Yodh, G. A. *Nature* **2011**, *476*, 308-311.
18. Petsi, J. A.; Kalarakis, N. A.; Burganos, N. V. *Chem. Eng. Sci.* **2010**, *65*, 2978-2989.
19. Park, J.; Moon, J. *Langmuir* **2006**, *22*, 3506−3513.
20. Xu, J.; Xia, J. F; Lin, Z. Q. *Angew. Chem. Int. Ed.* **2007**, *46*, 1860-1863.
21. Wikipedia page. http://en.wikipedia.org/wiki/File:Contact_angle.svg (accessed April 21, 2012).
22. Young, T. *Phil. Trans. R. Soc. Lond.* **1805**, *95*, 65–87.
23. Orejon, D.; Sefiane, K.; Shanahan, M. E. R. *Langmuir* **2011**, *27* (21), 12834–12843.
24. Shanahan, M. E. R.; Carré, A. *Langmuir* **1995**, *11*, 1396-1402.
25. Moffat, J. R.; Sefiane, K.; Shanahan, M. E. R. *J. Phys. Chem. B* **2009**, *113*, 8860-8866.
26. Maenosono, S.; Dushikin, C. D.; Saita, S.; Yamaguchi, Y. *Langmuir*, **1999**, *15*, 957-965.
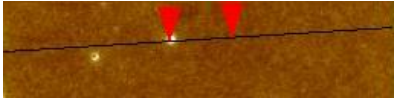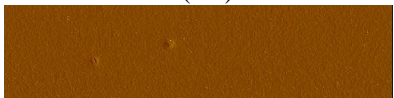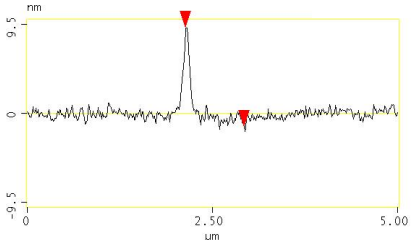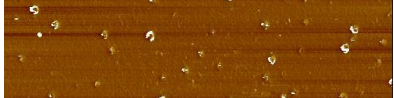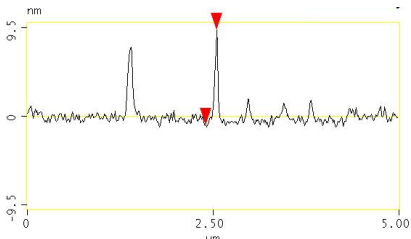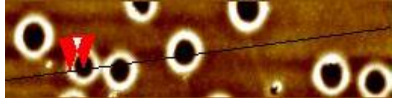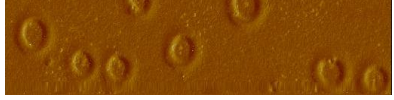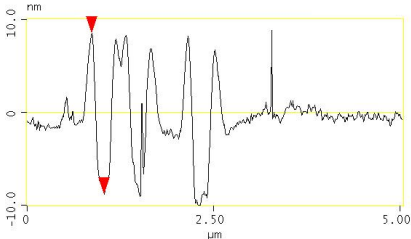
27. Xia, Y.; Gates, B.; Yin, Y.; Lu, Y. *Adv. Mater.* **2000**, *12*, 693-713.
28. Whitesides, M. G.; Grzybowski, B. *Science* **2002**, *295*, 2418-2421.
29. Thurn-Albrecht, T.; Schotter, J.; Kastle, A. C.; Emley, N.; Shibauchi, T.; Krusin-Elbaum, L.; Guarini, K.; Tuominen, T. M.; Russell, P. T. *Science* **2000**, *290*, 2126-2129.
30. Compton, D.; Comish, L.; van der Lingen, E. *Gold Bull*. **2003**, *36*, 10-16.
31. Faraday, M. *Philos. Trans. R. Soc. London, Ser. A* **1857**, *147*, 145-181.
32. El-Sayed, M. A. *Acc. Chem. Res.* **2001**, *34(4)*, 257-264.
33. Ghosh, S. K.; Pal, T. *Chemical Reviews*. **2007**, *107*, 4797-4862.
34. Daniel, M. C.; Astruc, D. *Chem. Rev.* **2004**, *104*, 293-346.
35. Kumar, S.; Grandhi, S. K.; Kumar, R. *Ind. Eng. Chem. Res.* **2007**, *46*, 3128-3136.
36. Murphy, C.J.; Gole, A. M.; Stone, J. W.; Sisco, P. N.; Alkilany, A. M.; Goldsmith, E. C. *Acc. of Chem. Res.* **2008**, *41*, 1721–1730.
37. Trudel, S. *Gold Bull*. **2011**, *44*, 3-13.
38. Kinge, S.; Crego-Calama, M.; Reinhoudt, N. C. *Chem. Phys. Chem.*, **2008**, *9*, 20-42.
39. Xia, D.; Li, D.; Luo, Y.; Brueck, J. R. *Adv. Mater.* **2006**, *18*, 930-933.
40. Wu, C. X.; Chi, F. L.; Fuchs, H. *Eur. J. Inorg. Chem.* **2005**, *18,* 3729-3733.
41. Hao, E.; Lian, Q. T. *Langmuir* **2000**, *16*, 7879-7881.
42. Lu, H. C.; Wu, Z. N.; Jiao, M. X.; Luo, Q. C.; Cao, X. W. *Chem. Commum.* **2003**, 1056-1057.
43. Rabani, E.; Reichman, R. D.; Geissler, L. P.; Brus, E. L. *Nature* **2003**, *426*, 271-274.
44. Kralchevsky, A. P.; Danov, D. K. *Nanoscience: Colloidal and Interfacial Aspects*, Chapter 15 (CRC Press, New York, 2010) p. 397-435.
45. Jordan, J.; Jacob, K. I.; Tannenbaum, R.; Sharaf, M. A.; Jasiuk, I. *Mater. Sci. Eng. A: Struct. Mater. Prop. Microstruct. Process.* **2005**, *393* (1-2), 1-11.
46. Alcoutlabi, M.; McKenna, G. B. J. Phys.: Condens. Matter 2005, *17*, R461-R524.
47. Brust, M.; Walker, M.; Bethell, D.; Schiffrin, D. J.; Whyman, R. *Chem. Commun.* **1994**, 801-802.
48. Brousseau, L. C., III; Novak, J. P.; Marinakos, S. M.; Feldheim, D. L. *Adv. Mater.* **1999**, *11*, 447-449.
49. Chechik, V.; Crooks, R. M. Langmuir, **1999**, *15*, 6364-6369.
50. Wu, C. K.; Hultman, K. L.; O'Brien, S.; Koberstein, J. T. *J. Am. Chem. Soc.* **2008**, *130*, 3516–3520.
51. Bae, K. S.; Lee, Y. S.; Hong, C. S. *React, Funct. Polym*. **2011**, *71*, 187-201.
52. Lin, H. L.; Liu, Y. F.; Yu, T. L.; Liu, W. H.; Rwei, S. P. *Polymer* **2005**, *46*, 5541-5549.
53. Mark, H. F.; Kroschwitz, J. I. In *Encyclopedia of Polymer Science and Technology*; Wiley-Interscience: New York, **1985**.

54. Toyoshima, K. In C.A. Finch, ed., *Polyvinyl Alcohol*, John Wiley & Sons, Inc., London, **1973**, p. 17-65, 339-389.

55. Zhang, H.; Penn, R. L.; Hamers, R. J.; Banfield, J. F. *J. Phys. Chem. B* **1999**, *103*, 4656-4662.

56. Nowicki, W. *Macromolecules* **2002**, *35*, 1424-1436.

57. Brewer, S. H.; Glomm, W. R.; Johnson, M. C.; Knag, M. K.; Franzen, S. *Langmuir* **2005**, *21*, 9303-9307.

58. Kozlov, M.; Quarmyne, M.; Chen, W.; McCarthy, T. J. *Macromolecules* **2003**, *36*, 6054-6059.

59. Kozlov, M.; Moon, I. S.; Smith, A. T.; McCarthy, T. J. *Polymer Preprints* **2003**, *44(2)*, 283.

60. Huang, S.; Sakaue, H.; Shingubara, S.; Takahagi, T. *Jpn. J. Appl. Phys.* **1998**, *37*, 7198–7201.

61. Huang, S.; Tsutsui, G.; Sakaue, H.; Shingubara S.; Takahagi, T. *Jpn. J. Appl. Phys.* **1999**, *39*, L473–L476.

62. Stainless Steel Tube &Pipe page. http://www.stainless-steel-tube.org/Stainless-Steel-Tubes-Surface-Roughness-Review-018.htm (accessed April 22, 2012).

63. Yockell-Lelievre, H.; Desbiens, J.; Ritcey, A. M. *Langmuir* **2007**, *23*, 2843-2850.

64. Polymer Crystallinity Page. http://faculty.uscupstate.edu/llever/Polymer%20Resources/Crystalline.htm (accessed April 22, 2012).
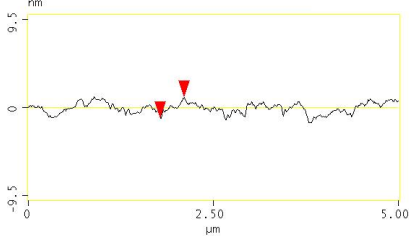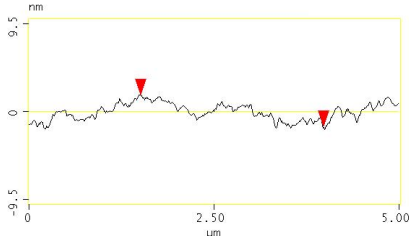
Appendix 1(a). AFM characterization of surface features after each step of reaction on silicon wafer substrates.
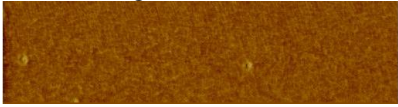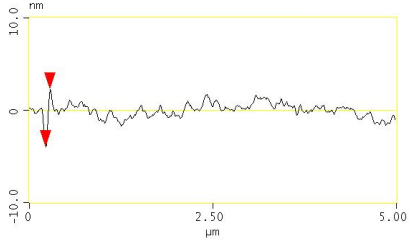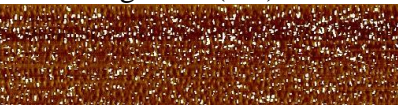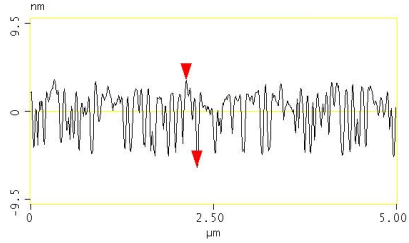
Surface Chemical Species	Contact Angle (°) (θ_A/θ_R)	AFM Images (5.0×1.25 μm): Height (top; scale: 20 nm) Phase (bottom; angle: 20°)	Section Analysis
Silane	Water: 113±2/92±2 NP Solution[*]: 111±3/90±2	Roughness (nm): 0.2 Thickness (nm): 0.6±0.1	
		Roughness (nm): 0.2 Thickness (nm): 0.7±0.1	
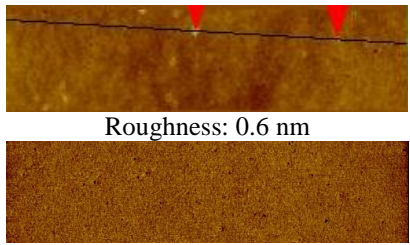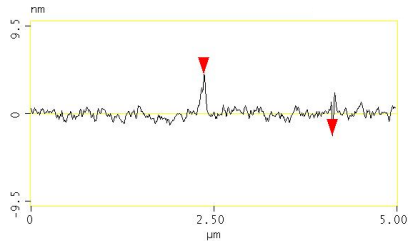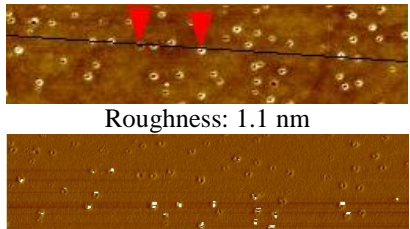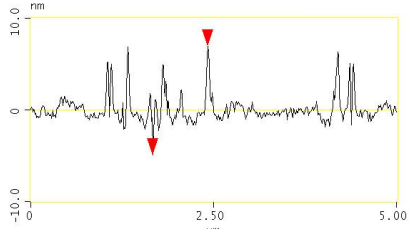
PVOH	Water: 57±2/16±2 NP Solution: 62±2/16±2	 Roughness (nm): 0.4 Thickness (nm): 3.2±0.6	
	Water: 41±2/16±2 NP Solution: 38±2/17±2	 Roughness (nm): 0.6	

HFBC	Water: 112±2/81±2 NP Solution: 111±3/74±2	 Roughness (nm): 0.6 Thickness (nm): 4.4±0.9	
	Water: 108±2/75±2 NP Solution: 110±5/58±2	 Roughness (nm): 1.3	
	Water: 109±2/69±4 NP Solution: 109±2/54±4	 Roughness (nm): 3.3	

Appendix 1(b). AFM characterization of surface features after each step of reaction on quartz substrates.
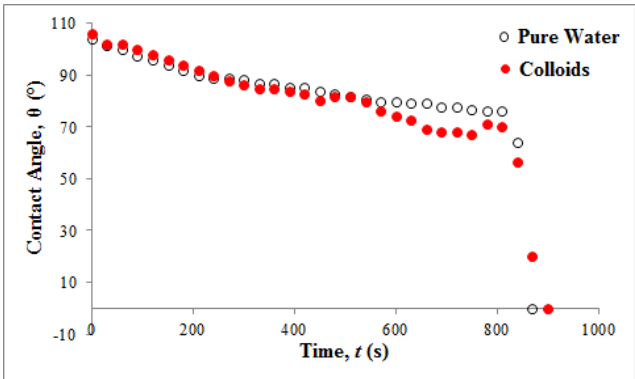
Surface Chemical Species	Contact Angle(°) (θ_A/θ_R)	AFM Images (5.0×1.25 μm): Height (top; scale: 20 nm) Phase (bottom; angle: 20°)	Section Analysis
Silane	Water: 110±2/77±2 NP Solution: 110±2/75±2	 Roughness (nm): 0.5 	
		 Roughness (nm): 0.7 	

PVOH	Water: 61±2/14±2 NP Solution: 61±4/14±2	 Roughness (nm): 0.7 	
	Water: 41±2/15.5±2 NP Solution: 36±2/8±2	 Roughness (nm): 2.1 	

HFBC	Water: 111±2/80±2 NP Solution: 110±2/74.5±2	 Roughness: 0.6 nm 	
	Water: 109±4/72.5±2 NP Solution: 107±2/63.5±2	 Roughness: 1.1 nm 	
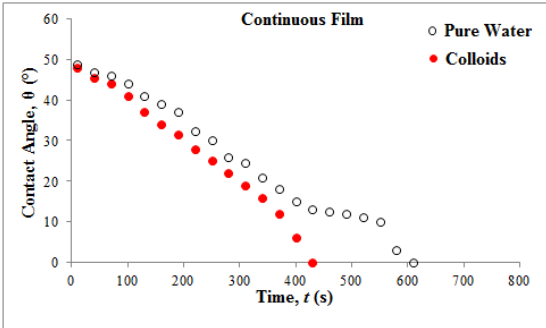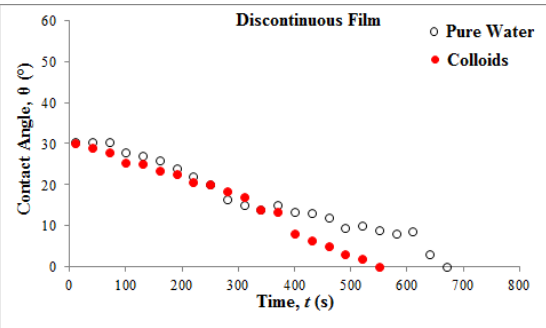
NP Solution[*]: The solution containing AuNPs was obtained after concentrating the original PVOH-AuNPs solution ten times.

Appendix 2. Deposit patterns (scale bar is 500 μm) and drying dynamics of sessile drops containing PVOH-AuNPs and pure water on silanized substrates.

Silane	Contact angle, θ (°), vs time (s)	Contact diameter, D (μm), vs time (s)
Silicon Wafer	Dynamic Contact Angle (θ_A/θ_R): Water: 113±2°/92±2° NP Solution: 111±3°/90±2° 	N/A

Quartz Slides	Dynamic Contact Angle (θ_A/θ_R): Water: $110\pm2°/77\pm2°$ NP Solution: $110\pm2°/75\pm2°$ 	
Glass Slides	Dynamic Contact Angle (θ_A/θ_R): Water: $109\pm2°/85\pm2°$ NP Solution: $106\pm2°/81\pm2°$ 	

Appendix 3. Deposit patterns (scale bar is 500 μm) and drying dynamics of sessile drops containing PVOH-AuNPs and pure water on substrates adsorbed with PVOH.

PVOH	Contact angle, θ (°), vs time (s)	Contact diameter, D (μm), vs time (s)
Silicon Wafer	Dynamic Contact Angle (θ_A/θ_R): Water: 57±2°/16±2° NP Solution: 62±2°/16±2° Dynamic Contact angle (θ_A/θ_R): Water: 41±2°/16±2° NP Solution: 38±2°/17±2° 	N/A

| Quartz Slides | Dynamic Contact Angle (θ_A/θ_R):
Water: $61\pm2°/14\pm2°$
NP Solution: $61\pm4°/14\pm2°$

Dynamic Contact Angle (θ_A/θ_R):
Water: $41\pm2°/16\pm2°$
NP Solution: $36\pm2°/8\pm2°$
 | |
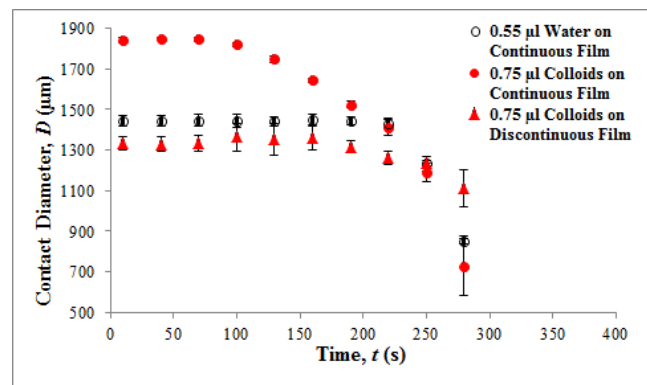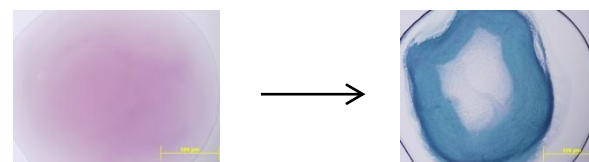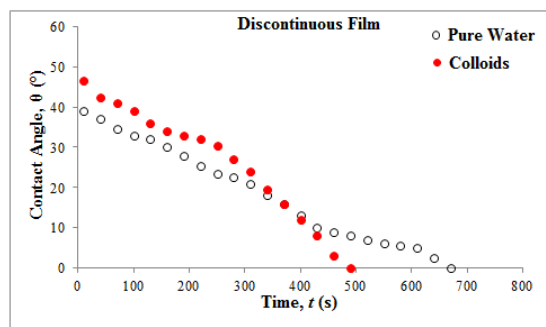
Glass Slides	Dynamic Contact Angle (θ_A/θ_R): Water: $61\pm2°/14\pm2°$ NP Solution: $60\pm2°/13\pm2°$ Dynamic Contact Angle (θ_A/θ_R): Water: $41\pm2°/14\pm3°$ NP Solution: $38\pm2°/14\pm2°$ 	
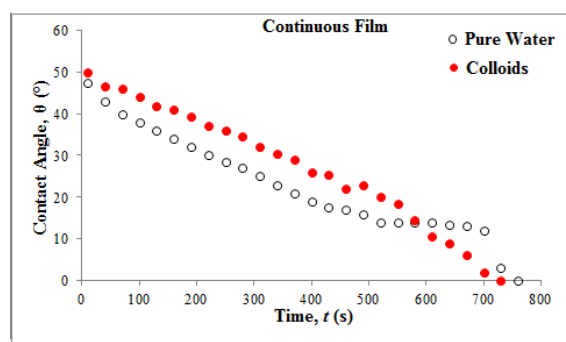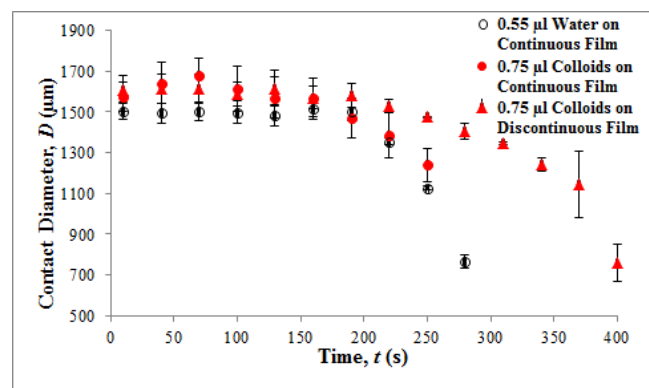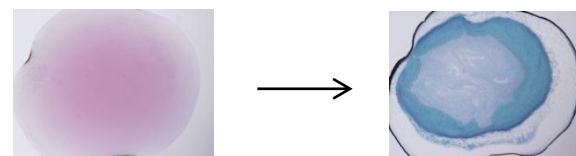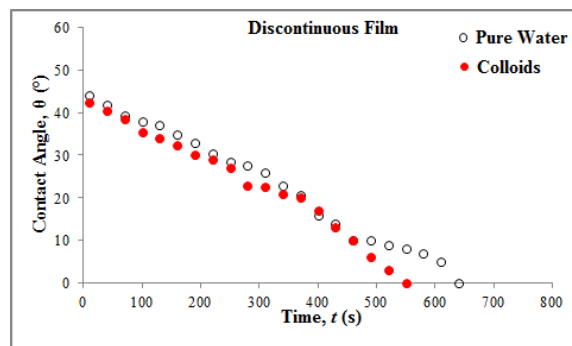
Appendix 4. Deposit patterns (scale bar is 500 µm) and drying dynamics of sessile drops containing PVOH-AuNPs and pure water on substrates reacted with HFBC.

Dynamic Contact Angle (θ_A/θ_R): Water: 112±2°/81±2° NP Solution: 111±3°/74±2° 	
Dynamic Contact Angle (θ_A/θ_R): Water: 108±2°/75±2° NP Solution: 110±5°/58±2° 	N/A
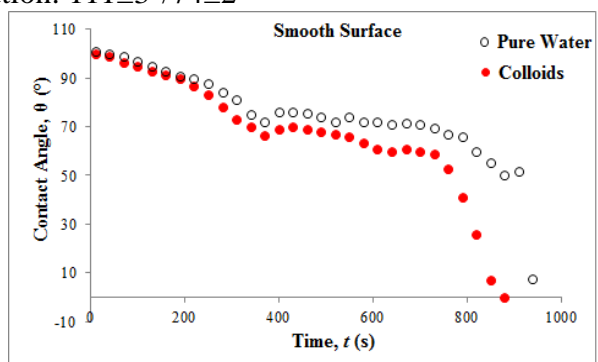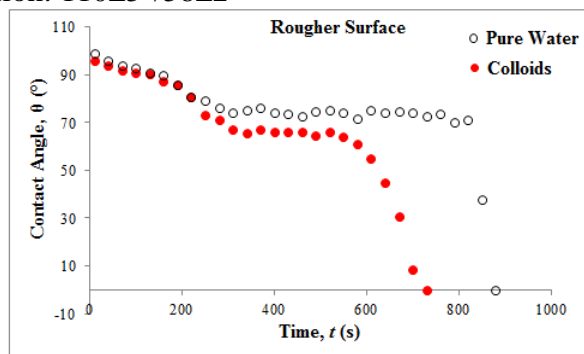
Dynamic Contact Angle (θ_A/θ_R):
Water: $109\pm2°/69\pm4°$
NP Solution: $109\pm5°/54\pm4°$
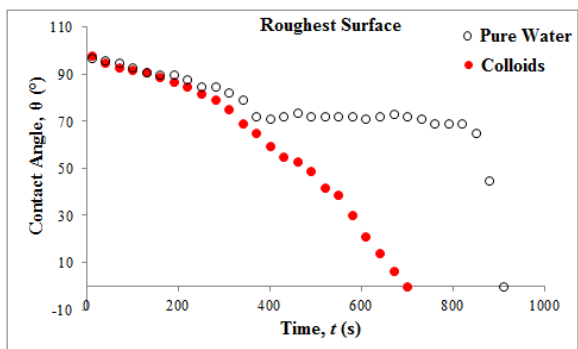
	Dynamic Contact Angle (θ_A/θ_R): Water: 111±2°/80±2° NP Solution: 110°±2/74±2°	
Quartz Slides		
	Dynamic Contact Angle (θ_A/θ_R): Water: 109±4°/72±2° NP Solution: 107±2°/64±2° N/A	
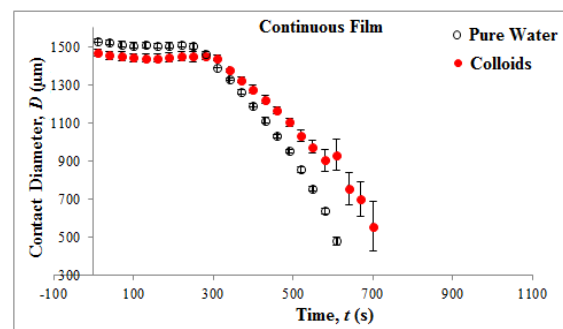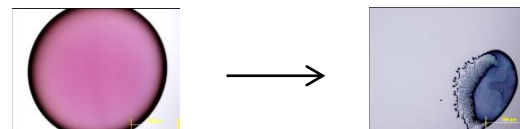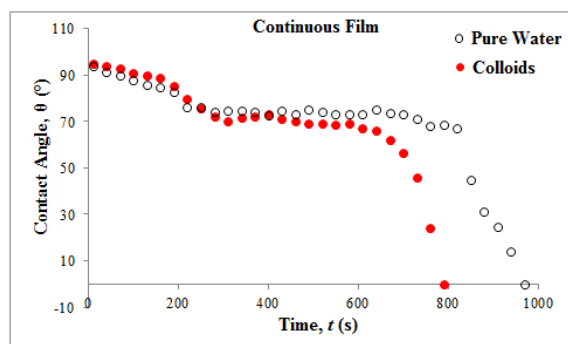
Glass Slides	Dynamic Contact Angle (θ_A/θ_R): Water: $109\pm2°/79\pm2°$ NP Solution: $110\pm2°/75\pm2°$ 	